AGU PUBLICATIONS

Geochemistry, Geophysics, Geosystems

RESEARCH ARTICLE
10.1002/2017GC007186

Arctic Deep Water Ferromanganese-Oxide Deposits Reflect the Unique Characteristics of the Arctic Ocean

James R. Hein[1], Natalia Konstantinova[2], Mariah Mikesell[1], Kira Mizell[1,3], Jessica N. Fitzsimmons[4], Phoebe J. Lam[3], Laramie T. Jensen[4], Yang Xiang[3], Amy Gartman[1], Georgy Cherkashov[5], Deborah R. Hutchinson[6], and Claire P. Till[7]

[1]U.S. Geological Survey, PCMSC, Santa Cruz, CA, USA, [2]Institute of Earth Sciences, St. Petersburg State University, St. Petersburg, Russia, [3]Ocean Sciences, University of California at Santa Cruz, Santa Cruz, CA, USA, [4]Department of Oceanography, Texas A&M University, College Station, TX, USA, [5]VNIIOkeangeologia, St. Petersburg, Russia, [6]U.S. Geological Survey, Woods Hole Science Center, Woods Hole, MA, USA, [7]Chemistry Department, Humboldt State University, Arcata, CA, USA

Abstract Little is known about marine mineral deposits in the Arctic Ocean, an ocean dominated by continental shelf and basins semi-closed to deep-water circulation. Here, we present data for ferromanganese crusts and nodules collected from the Amerasia Arctic Ocean in 2008, 2009, and 2012 (HLY0805, HLY0905, and HLY1202). We determined mineral and chemical compositions of the crusts and nodules and the onset of their formation. Water column samples from the GEOTRACES program were analyzed for dissolved and particulate scandium concentrations, an element uniquely enriched in these deposits. The Arctic crusts and nodules are characterized by unique mineral and chemical compositions with atypically high growth rates, detrital contents, Fe/Mn ratios, and low Si/Al ratios, compared to deposits found elsewhere. High detritus reflects erosion of submarine outcrops and North America and Siberia cratons, transport by rivers and glaciers to the sea, and distribution by sea ice, brines, and currents. Uniquely high Fe/Mn ratios are attributed to expansive continental shelves, where diagenetic cycling releases Fe to bottom waters, and density flows transport shelf bottom water to the open Arctic Ocean. Low Mn contents reflect the lack of a mid-water oxygen minimum zone that would act as a reservoir for dissolved Mn. The potential host phases and sources for elements with uniquely high contents are discussed with an emphasis on scandium. Scandium sorption onto Fe oxyhydroxides and Sc-rich detritus account for atypically high scandium contents. The opening of Fram Strait in the Miocene and ventilation of the deep basins initiated Fe-Mn crust growth ~15 Myr ago.

Key Points:
- The unique characteristics of Arctic Ocean Fe-Mn crusts and nodules reflect the unique characteristics of the Arctic Ocean and surrounding areas
- Arctic Ocean ferromanganese crusts and nodules are textually and compositionally unique within the global ocean
- Scandium is concentrated only in Arctic Ocean crusts and nodules as the result of sorption on matrix minerals and input of Sc-rich detritus

Supporting Information:
- Supporting Information S1
- Table S1
- Table S2
- Table S3
- Table S4
- Table S5
- Table S6
- Table S7
- Table S8
- Table S9

Correspondence to:
J. R. Hein,
jhein@usgs.gov

Citation:
Hein, J. R., Konstantinova, N., Mikesell, M., Mizell, K., Fitzsimmons, J. N., Lam, P. J., . . . Till, C. P. (2017). Arctic deep water ferromanganese-oxide deposits reflect the unique characteristics of the Arctic Ocean. *Geochemistry, Geophysics, Geosystems*, *18*, 3771–3800. https://doi.org/10.1002/2017GC007186

Received 10 AUG 2017
Accepted 12 SEP 2017
Accepted article online 21 SEP 2017
Published online 8 NOV 2017

1. Introduction

1.1. Ferromanganese Deposits

Ferromanganese (Fe-Mn) oxide crusts grow on rock surfaces throughout the global ocean at water depths from about 400 to 7,000 m (e.g., Hein et al., 2000). Fe-Mn crusts develop by precipitation from ambient bottom waters and accretion of colloids onto rock surfaces. Fe-Mn nodules studied here form by the same process, and differ by accretion of the oxides around a nucleus on sediment. Fe-Mn crusts and nodules are and have been the focus of extensive research for four reasons: (1) they have a resource potential for many critical and base metals (e.g., Hein et al., 2013a), (2) they play a role in the geochemical balance of the oceans (e.g., Hein & Koschinsky, 2014), (3) they contribute to our understanding of chemical sedimentology and geochemical processes (e.g., Halbach et al., 1983; Wen et al., 1997), and (4) the condensed stratigraphic sections that comprise crusts and nodules record the Cenozoic history of seawater through changes in the composition of their growth layers (e.g., Frank et al., 1999; Nielsen et al., 2009). The latter two of these four reasons are the focus of this paper.

The composition of Fe-Mn crusts and nodules varies not only temporally within individual samples, but also spatially on global, regional, and local scales. Notable differences in mineralogy and chemical composition occur in open-ocean crusts compared to those that form along continental margins and other areas where upwelling and primary productivity are high. As a result, continent proximal crusts that form in a more intense and extensive Oxygen Minimum Zone (OMZ) (Conrad et al., 2017) differ from Fe-Mn crusts that form in the relatively weak OMZs found around open-ocean seamounts.

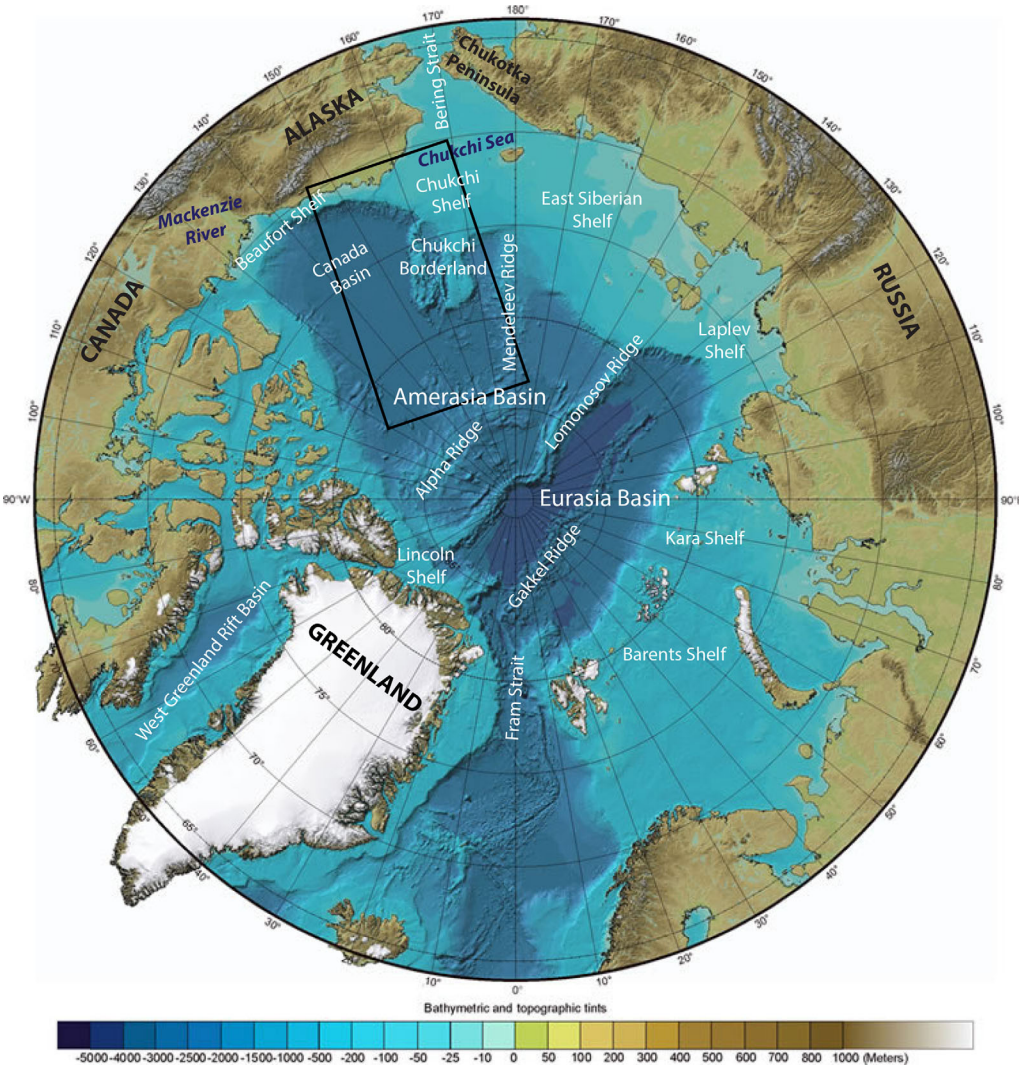

Figure 1. Regional location map and bathymetry of the Arctic Ocean with the study area delineated by the black rectangle (Base map, IASC, 2004).

Fe-Mn crusts collected from seamounts in the Pacific Ocean have been extensively studied, and Atlantic Ocean and Indian Ocean crusts are less well studied in part because the Atlantic and Indian Oceans are dominated topographically by spreading centers rather than abundant old seamounts where thick crusts predominantly grow. Until recently, Fe-Mn crusts from the Arctic Ocean had not been studied because collection was difficult when ice cover was thick and more extensive. Now, United States and Russian research programs are studying Fe-Mn crusts and nodules collected from the Amerasia Basin (Figures 1 and 2) (Hein et al., 2012b; Hein et al., 2013b; Konstantinova et al., 2017). Fe-Mn crusts were noted in a few previous studies of samples from Mendeleev Ridge, which are summarized by Konstantinova et al. (2017). Fe-Mn micronodules from Alpha Ridge were collected and studied in some detail by Winter et al. (1997). The 29 micronodules (50–300 μm diameter) studied formed by two processes: hydrogenesis, where metals precipitate from ambient seawater, and diagenesis, where metals derive from redox cycling in the sediment. In addition, Clark et al. (1980) noted sand-sized Fe-Mn oxide micronodules in sediment cores from the Canada Basin and Alpha Ridge from water depths of 1,069–3,820 m. Those micronodules formed through various stratigraphic intervals from late Miocene through Holocene by diagenetic processes within the sediment. Our study includes a broad area and a large collection of Fe-Mn crusts and nodules that formed by hydrogenesis. Fe-Mn nodules are not abundant and were collected from only 2 of the 10 sites where Fe-Mn crusts were collected.

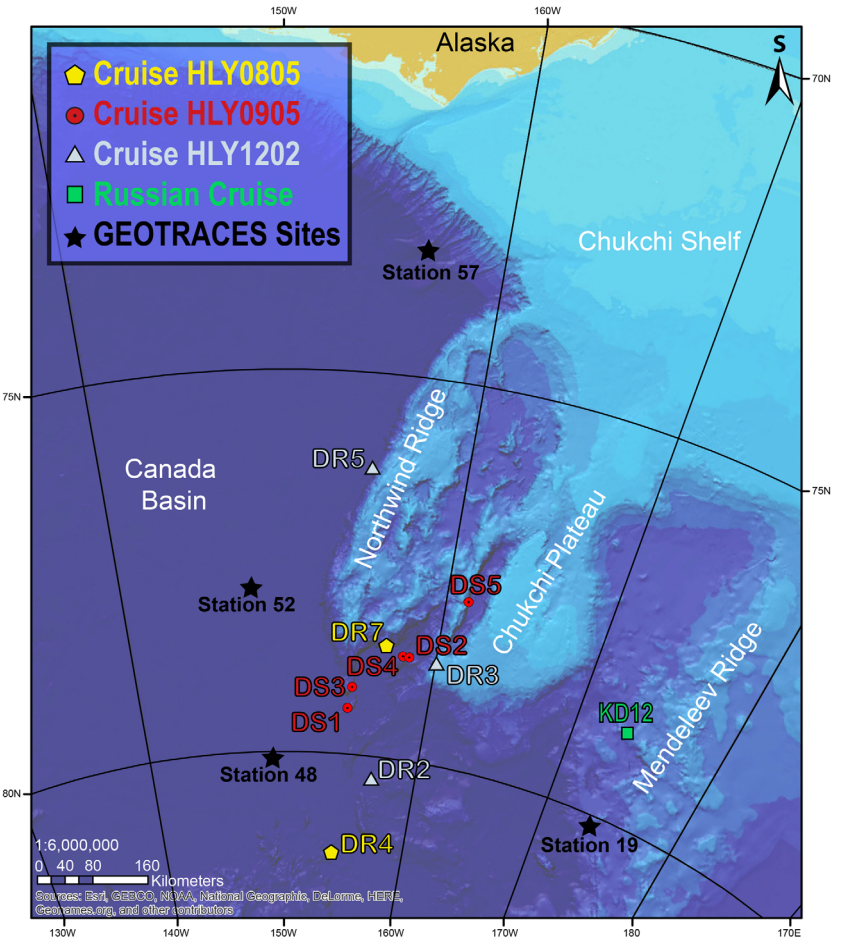

Figure 2. Map of the Chukchi Borderland north of Alaska, Amerasia Arctic Ocean, with dredge sites from three USCGC *Healy* cruises and one Russian cruise. Locations of four GEOTRACES sites for which we present dissolved and particulate scandium data are indicated. Dredge site DR4 is on the lower flank of Alpha Ridge, which occurs mostly to the north of the boundary of this figure. Color variations in bathymetry are relative changes in water depth with progressively darker colors reflecting progressively deeper water. The Chukchi shelf averages 41 m water depth and the Canada Basin averages ~3,800 m.

1.2. Arctic Ocean Background

The Arctic Ocean is divided into the Eurasia and Amerasia Basins, separated by the Lomonosov Ridge (Figure 1). Atlantic seawater is transported through the Fram Strait into the Eurasia Basin, and then through a 2,000 m deep sill at the Asian end of Lomonosov Ridge and into the Amerasia Basin (Björk et al., 2007; Timmermans et al., 2005). The Fram Strait opened to deep water exchange about 17 Myr ago (e.g., Jakobsson et al., 2007). Pacific seawater is transported through the Bering Strait in the Amerasia Arctic at a sill depth of about 50 m, which opened about 5.4 Myr ago (e.g., Gladenkov et al., 2002). Pacific seawater and return water from the Atlantic are transported through a sill at the North America end of Lomonosov Ridge as well as through a sill along the central ridge at 1,870 m depth (Jones et al., 1995). The deep Canada Basin in the Amerasia Arctic Ocean is semi-closed to ocean-wide circulation, although it has also been proposed that the deep water is continuously renewed (Timmermans et al., 2005). Our study area borders the Canada Basin and includes the Chukchi Borderland and Mendeleev and Alpha Ridges (Figures 1 and 2).

The Arctic Ocean has many unique characteristics compared to the other oceans. For example, the Arctic Ocean comprises ~1.4% of the global ocean volume and receives 10% of the world river discharge (Jakobsson, 2002; van der Loeff et al., 2012). Approximately 53% of the Arctic Ocean is underlain by an extensive continental shelf, which effectively produces the shallowest mean water depth (1,201 m) compared to the other oceans (Jakobsson, 2002). Freezing along the shelf produces brines that because of their high-density sink and move shelf bottom waters seaward to form the halocline and also contribute to deeper water masses; at times in the past, this dense water had descended down through the Arctic Intermediate water

Table 1
Location of Dredge Sites Listed From North to South (See Figure 2)

Cruise ID	Dredge	Water depth (m)	Latitude (N)	Longitude (W)
HLY0805	DR4	3,467	81.31	153.99
HLY1202	DR2	3,800	80.32	156.75
HLY0905	DS1	3,600	79.40	154.45
HLY0905	DS3	3,300	79.12	154.60
HLY1202	DR3	1,605	78.70	160.05
HLY0905	DS4	2,200	78.66	158.25
HLY0905	DS2	2,400	78.65	157.83
HLY0805	DR7	3,400	78.53	156.68
HLY0905	DS5	2,100	77.81	161.35
HLY1202	DR5	3,851	76.26	154.74

(AIW) (Haley et al., 2008) and into the deep basins by density flows triggered by the brines along the continental slope (e.g., Jones et al., 1995).

2. Samples and Methods

2.1. Sample Collection

Fe-Mn crusts and nodules were selected from dredge hauls collected during the 2008, 2009, and 2012 cruises (HLY0805, HLY0905, and HLY1202) of the USCGC icebreaker *Healy*. From north to south, the Chukchi Borderland samples studied here are from dredge hauls DR4 (Alpha Ridge), DR2, DS1, and DS3 (Pozharsky Seamount), DR3 (Chukchi Plateau), DS4 and DS2 (Healy Seamount), DR7, DS5 (Egiazarov Trough), and DR5 (Northwind Escarpment) collected at water depths ranging from 1,605 to 3,851 m (Figure 2 and Table 1); topography at sites DR2 and DR7 do not have official names. These 10 sites represent a variety of topographic settings, rock types, and geologic formations (see below). Dredges generally targeted steep slopes, so crusts occurring on gentler slopes, where more continuous crust pavements might occur, were not sampled.

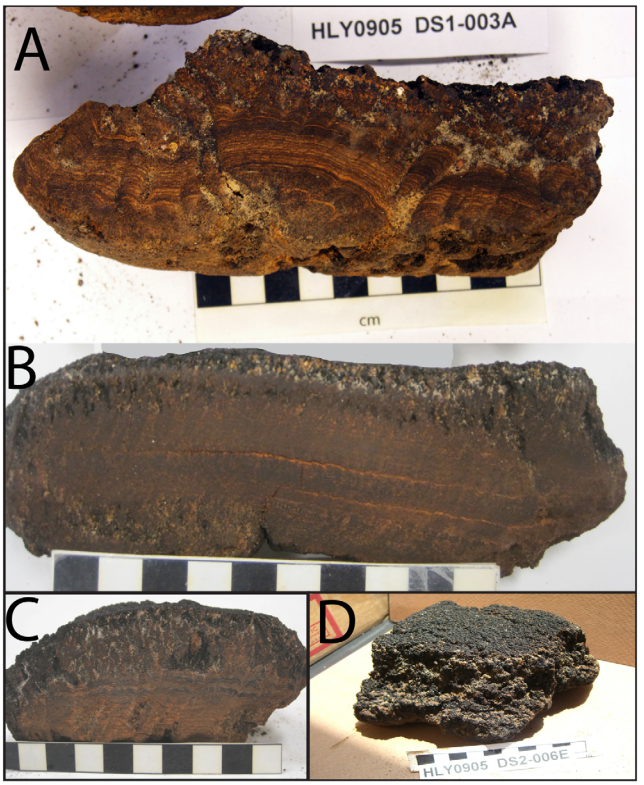

Figure 3. Photographs of cut surfaces showing stratigraphic layers in Fe-Mn crusts (a) HLY0905 DS1–003A, (b) HLY1202 DR2-001D, (c) HLY1202 DR5-D-D, and (d) uncut crust HLY0905 DS2–006E; note centimeter scale in each frame.

Crusts selected for analyses range in thickness from 6 mm (HLY12022 DR3–043-BLK) to 86 mm (HLY1202 DR5-D-C). Surface textures are porous granular, vuggy, and microbotryoidal, in contrast to crusts from elsewhere in the global ocean that typically vary between botryoidal and smooth. Columnar, botryoidal, laminated, and mottled layers comprise the Arctic Fe-Mn crust stratigraphic sections. No uniform sequence of textures is evident and all thick crusts are composed of three or four distinct macroscopic layers (Figure 3). Crust layers analyzed were separated along macroscopic boundaries so that the entire crust stratigraphic section (thickness) was sampled.

Substrate rock for crust DR7–014G, a Fe-Mn-oxide coated pebble, is altered sandstone; the substrate for crusts DS3–009, DS3–060C, DS4-003A, DS4-003C, DS4-004, and DS4–005 is basalt. Crusts DS1–011 and DS5–041 have metamorphic rock substrates with oriented and stretched quartz grains. The substrate rock on which all the other crusts grew was absent.

Trace-metal-clean seawater samples were collected on the GN01 Arctic and the GP16 South Pacific U.S. GEOTRACES cruises using the U.S. GEOTRACES sampling system of Teflon-coated GO-Flo bottles (Cutter & Bruland, 2012). Dissolved metal samples were filtered through a 0.2 μm Acropak-200 capsule filter (Pall) under ~0.7 atm pressure of HEPA-filtered air. Filtered seawater samples were collected into acid-

cleaned, low-density polyethylene (LDPE) plastic bottles, which were filled after three 10% volume rinses. Samples were acidified to 0.012 *M* hydrochloric acid concentration, using ultrapure acid (Optima, Fisher Scientific) for the Arctic samples and were acidified to 0.024 *M* with quartz-distilled HCl for the southeast Pacific samples. All samples were stored acidified for at least 6 months prior to analysis.

Size-fractionated (0.8–51 μm; >51 μm) particulate samples were also collected on the GN01 cruise using modified dual-flow McLane Research in *situ* pumps deployed on a metal-free Hytrel-coated Vectran line (Ohnemus & Lam, 2015). Full water column profiles of up to 24 depths were sampled over 2–3 casts of eight pumps each.

2.2. Methods

X-ray diffraction mineralogy was completed using a Philips X-ray diffractometer (XRD) with CuKα radiation and graphite monochromator run from 4° to 70° 2θ at 40 kV and 45 mA (supporting information Table S1). Digital scan results were analyzed using Philips X'pert HighScore to measure X-ray reflections and identify possible mineral compositions. The identification of minerals was constrained using chemical composition. Semi-quantitative mineral percentages were calculated by using peak intensities and weighing factors relative to quartz set as 1 (Cook et al., 1975; Hein et al., 1988). The detection limit for each mineral falls between about 0.2% and 1.0%, except for the poorly crystalline manganese minerals, for which the detection limits are as high as 10%.

A Tescan Vega3 Scanning Electron Microscope (SEM) was used at operating conditions of 30 kV and 15 nA for imaging; the EDS microprobe chemistry and element mapping was done using a JEOL 8900 operating at 15 kV and 40 nA for quantitative analyses of oxides; counting times were 30 s peak and 15 s background.

The chemical composition of Fe-Mn crusts was determined at SGS Laboratories, Canada: the 10 major elements were determined by X-Ray Fluorescence (XRF) on borate fused disks; Cs, Cu, Mo, Ni, V, Zr, and Rare Earth elements plus Y (REY) were determined by Inductively Coupled Plasma Mass Spectrometry (ICP-MS) using lithium-metaborate fused disks; Ag, As, Ba, Be, Bi, Cd, Co, Cr, Ga, Ge, Hf, In, Li, Nb, Pb, Rb, S, Sb, Sc, Sn, Sr, Ta, Th, Tl, U, W, and Zn by ICP-MS using a four-acid digest; Te and Se were determined by hydride generation and graphite furnace Atomic-Absorption Spectrometry (AAS); Hg by cold vapor AAS; H_2O^- by gravimetric analysis, H_2O^+ by penfield-infrared; and Cl by specific-ion electrode. Reproducibility was better than 5% for all elements except Ta, Ba, Ag, Tb, and H_2O^+, which range from 5% to 8%, and Sn, 12%. Accuracy is better than 5% for Si, Fe, Al, Mg, Y, Mn, Tm, Gd, K, La, Li, Pr, Yb, Bi, Ho, Th, P, Tb, Cl, Sr, Ce, Sb, Dy, Na, and Eu; 5%–7% for Sm, Lu, Er, Hg, Hf, In, Nb, Nd, Ba, Rb, Sn, Ca, As, and W; 7%–10% for Te, Ag, U, Zr, Ti, Co, Ni, and Cs; and 10%–15% for the others, except Ta and Ga are 18% and 20% respectively.

Carbon analysis was performed at the USGS by combustion, acidification, and coulometric detection using a UIC CM5015 coulometer, UIC CM5200 furnace, and UIC CM5230 acid digester. Total carbon, total inorganic carbon, and percent $CaCO_3$ were determined as percent dry weight, using procedures modified from Engleman et al. (1985).

Analyses for dissolved Sc (dSc) in Arctic GEOTRACES water column profile sample were made using an offline adaptation of the SeaFAST pico metal preconcentration system (Lagerström et al., 2013), which extracts metals onto Nobias PA1 chelating resin at pH 6.5. Sample eluent was analyzed for Sc in medium resolution on a Thermo Fisher Element XR ICP-MS at the R. Ken Williams Radiogenic Laboratory, Texas A&M University. Analyses of dSc in the southeast Pacific GEOTRACES profiles used the method of Biller and Bruland (2012) with adaptations described in Parker et al. (2016), which is an offline preconcentration method at pH 6.0 using the same chelating resin and type of ICP-MS (ICP-MS at University of California Santa Cruz).

Small Size Fraction (SSF; 0.8–51 μm) particle samples from GEOTRACES were digested using a refluxing digestion method that used a 50% HNO_3/10% HF (v/v) mixture on a hotplate (Cullen & Sherrell, 1999; Ohnemus et al., 2014; Planquette & Sherrell, 2012). Certified Reference Materials were run routinely alongside the samples to assure the quality of each digestion. Diluted digest solutions were analyzed for a suite of elements including Sc, Al, Fe, and Mn by high-resolution ICP-MS (Element XR, Thermo Scientific) at the UCSC Plasma Analytical Facility. An internal standard was used to correct for drift and matrix effects, and concentrations were quantified using mixed external standard curves (Heller et al., 2017).

REY plots were normalized to both chondrites (Anders & Grevesse, 1989) and Post-Archean Australian Shale (PAAS) (McLennan, 1989). The Ce anomaly (Ce_{SN}) was calculated as $Ce_{SN} = 2Ce_{SN}/(La_{SN}+Pr_{SN})$ with PAAS-normalized values.

The Pearson correlation coefficient was used to calculate matrices for the chemical data to measure the strength of linear dependence between two variables. Statistical significance will be specified at either a 99% or 95% Confidence Level (CL). Q-mode factor analysis was used to examine element relationships and calculations were run in MatLab (see Pisias et al., 2013) to identify common groups of elements referred to as factors. On the basis of X-ray diffraction mineralogy and element correlations, we interpret each factor to represent a particular mineral or group of minerals in the Fe-Mn crusts and elements in that factor to be contained in that mineral or mineral group. This links mineralogy that relates to environmental conditions to element concentrations that in part reflect different sources. For Q-mode factor analysis, each variable percentage was scaled to the percent of the maximum value before the values were row-normalized and cosine-theta coefficients calculated. Factors were derived from orthogonal rotations of principal component eigenvectors using the Varimax method (Klovan & Imbrie, 1971). All communalities are $\geq$0.9, an index of the efficiency of a reduced set of factors to account for the original variance.

3. Results

3.1. XRD Mineralogy

The XRD mineralogy is fairly uniform for the crusts and nodules collected throughout the study area. With rare exceptions, Fe minerals are dominant and Mn minerals occur in somewhat lower abundances (supporting information Table S1). The Fe minerals include various polymorphs of crystalline FeO(OH), including lepidocrocite, goethite, and feroxyhyte, as well as ferrihydrite and X-ray amorphous Fe hydroxide phases (see also Konstantinova et al., 2017). Manganese minerals include predominantly δ-MnO_2 (vernadite), birnessite, and 10 Å manganates (todorokite, buserite, and asbolane), and rarely ramsdellite (MnO_2), in nodule DR7–014D. Heating four samples to 300°C for 24 h indicates that the predominant 10 Å manganate is todorokite (Wegorzewski et al., 2015), with minor buserite. Quartz, plagioclase, and K-feldspar occur in moderate to minor amounts in most samples (supporting information Table S1). Mica occurs in samples from dredge sites DS1 and DR3, and clay minerals (kaolinite, illite, tosudite, smectite, and rectorite) occur in many Fe-Mn crust samples throughout the region; chlorite is also common in some substrate rocks. Dolomite occurs in samples from three dredge sites (DR2, DR4, and DR5).

3.2. Geochemistry

Chemical data were analyzed statistically in four groupings: All samples (n = 101), bulk Fe-Mn crust samples (n = 50), crust layers (n = 44), and Fe-Mn nodules (n = 7). Of the 50 bulk crusts, eight compositions were not measured directly, rather their bulk compositions were determined using the chemical data for megascopic layers through the entire crust thickness and weighting layer chemical data by layer thickness. Statistics for the bulk crusts, crust layers, and combined data set are very similar in mean element concentrations (Table 2 and supporting information Tables S2–S4). Compositions of the nodules fall within the range for crust layers and bulk crusts, and since the genesis of the crusts and nodules are the same (see below), and water depths of collection are the same (Table 1), we include the nodule chemical data with the crust data in the combined data set.

A key characteristic of the Arctic Fe-Mn deposits is the uniquely high Fe contents relative to Mn (Fe/Mn ratio), consistent with the mineralogy (supporting information Tables S1 and S5); the high Fe/Mn ratios are due to anomalously low Mn contents, compared to crusts from elsewhere in the global ocean (Hein et al., 2013a). The mean Fe/Mn for all samples is 2.67 (range 1.17–5.69), which is higher than other crusts (means 0.74–1.44) from the global ocean (Hein et al., 2013a; Hein & Koschinsky, 2014). Another key finding is that mean As, Hg, Li, Sc, Th, and V contents are enriched in the Arctic hydrogenetic Fe-Mn crusts much more so than in hydrogenetic crusts from open-ocean sites or from the California margin. The mean contents for the entire data set are: As 559 ppm, Li 89 ppm, Sc 47 ppm, Th 62 ppm, and V 936 ppm, compared to mean data for crusts from other areas in the global ocean of As 207–393 ppm, Li 2.9–33 ppm, Sc 6.6–16 ppm, Th 11–56 ppm, and V 613–849 ppm (Hein & Koschinsky, 2014; Hein et al., 2013a). Sc is highly enriched relative to the average content of the Earth's crust (14–16 ppm) and is enriched only in Arctic crust and nodule samples (Figure 4).

For the combined data set, Mg, Ti, Fe, and Na contents vary only slightly, less than by a factor of two, and P and Al by 2–2.5; in contrast, Si varies the most, by a factor of 7.6. The mean contents of Fe and Mn for the 50 bulk crusts range between 15.9 wt % and 23.1 wt % (mean 19.8%) and 4.85% and 14.6% (mean 7.70%) respectively (supporting information Table S5). Al (3.56%–7.80%, mean 6.29%) is rather uniform throughout

Table 2
Statistics for the Combined Sample Geochemical Data Set

	N	Mean	Median	StDev	Min	Max
Fe (wt%)	99	19.9	20.0	2.11	12.5	24.0
Mn	99	7.67	7.01	2.72	3.78	16.7
Fe/Mn	99	2.60	2.74	1.03	1.17	5.69
Si	99	11.1	11.5	2.67	2.40	18.3
Al	99	6.32	6.44	1.11	3.56	8.74
Si/Al	99	1.75	1.73	0.52	0.67	4.79
Ca	99	1.18	1.11	0.34	0.70	2.07
Mg	99	1.66	1.64	0.15	1.34	2.15
Na	99	1.61	1.58	0.22	1.16	2.28
K	99	1.14	1.17	0.23	0.51	1.61
Ti	99	0.36	0.36	0.03	0.29	0.52
P	99	0.54	0.54	0.07	0.33	0.72
H_2O^-	101	10.0	9.50	3.10	6.00	20.5
H_2O^+	57	8.05	8.80	2.93	0.60	12.1
LOI	99	23.3	22.7	3.14	18.3	33.6
Ag (ppm)	100	<0.27	<0.22	0.33	<0.03	2.3
As	101	559	547	101	360	809
Ba	101	451	434	71	325	672
Be	101	5.8	5.8	1.2	3.1	9.1
Bi	101	3.9	3.2	2.3	1.3	15
Cd	101	3.5	3.3	1.0	1.8	7.2
Cl	74	>12,694	>12,580	3,183	6,942	>19,784
Co	101	1,452	1,246	875	441	5,372
Cr	101	43	43	11	19	80
Cs	92	3.0	3.1	0.86	1.1	5.1
Cu	92	643	638	97	424	957
Ga	101	13	14	4.2	1.0	23
Ge	9	0.69	0.69	0.14	0.34	0.81
Hf	74	10	10	2.0	6.7	15
Hg (ppb)	99	<54	<37	52	<6.8	219
In (ppm)	101	0.33	0.34	0.06	0.22	0.49
Li	101	89	83	38	30	292
Mo	92	209	190	73	124	495
Nb	101	39	34	19	19	140
Ni	92	2,289	2,039	1,240	864	6,116
Pb	101	233	196	131	93	882
Rb	101	47	49	12	16.6	72
S	101	2,693	2,602	623	1,708	4,870
Sb	101	48	41	19	27	108
Sc	101	47	48	7.4	23	62
Se	99	<0.64	<0.65	0.23	<0.21	1.2
Sn	101	8.4	7.1	8.1	2.5	79
Sr	101	476	422	169	280	1,059
Ta	74	0.85	0.92	0.29	0.10	1.5
Te	98	16	14	9.6	6.6	55
Th	101	62	58	19	41	161
Tl	101	83	78	37	12	233
U	101	11	11	1.9	6.1	17
V	92	936	921	130	657	1,247
W	101	49	43	20	26	134
Zn	101	341	339	54	213	468
Zr	92	428	422	51	316	765
La	101	150	123	77.1	85.5	448
Ce	101	849	771	328	451	2,018
Pr	101	42.2	34.8	21.9	22.6	124
Nd	101	170	142	86.1	91.0	479
Sm	101	42.6	36.0	20.8	23.9	120
Eu	101	10.8	9.28	4.57	6.40	28.9
Gd	101	47.0	41.7	18.1	28.6	117

Table 2. *(continued)*

	N	Mean	Median	StDev	Min	Max
Tb	101	7.81	7.07	2.94	4.61	18.7
Dy	101	44.6	40.4	15.2	27.9	102
Y	101	192	176	55.0	132	375
Ho	101	9.00	8.24	2.94	5.80	19.7
Er	101	24.2	22.1	7.40	16.1	50.3
Tm	101	3.74	3.44	1.13	2.13	7.66
Yb	101	22.7	20.9	6.65	13.3	46.0
Lu	101	3.57	3.30	1.04	2.26	6.99
ΣREY	101	1,619	1,437	638	929	3,927
%HREY	101	23%	23%	2%	17%	27%

Note. LOI, loss on ignition at 1,000°C; ∑REY, sum of rare earth elements plus yttrium; %HREY, percent of heavy REY (Eu – Lu + Y) of the total sum of REY.

the study area in bulk crusts, varying by a factor of 2.2, whereas Si (3.96%–14.7%, mean 11.0%) varies by a factor of 3.7; Si and Al are highest in dredge DR5 crust samples, the most southern, continent proximal site.

The metals traditionally considered of greatest economic potential for Fe-Mn crusts and nodules (Co, Ni, Cu) vary throughout the study area, with a mean Co + Cu + Ni content of 0.45% and maximum of 1.02% compared to a combined mean for the other oceans of 1.04% (Hein et al., 2013a). Co and Ni contents are highest in dredge DR3 samples DR3–047B and DR3-036, 0.36% (bulk crust mean 0.15%) and 0.56% (bulk crust mean 0.23%), respectively. Dredge DR3 is the shallowest water site, 1,605 m, and Co and Ni are known to increase with decreasing water depth (e.g., Hein et al., 2000). Sample DS3–060C has the highest Cu content, 0.1% (mean bulk crusts 0.07%), which is from 3,300 m water depth. Cu generally increases with increasing water depth (e.g., Hein et al., 2000).

Other elements of potential economic interest that occur in high concentrations in bulk crusts include (maximum, mean): total REY contents (ΣREY 0.37%, 0.16%), V (1,196 ppm, 936 ppm), Mo (468 ppm, 213 ppm), W (118 ppm, 50 ppm), Nb (93 ppm, 40 ppm), and Sc (60 ppm, 46 ppm). Additional elements with high concentrations are Tl (296 ppm, 91 ppm) and Th (111 ppm, 63 ppm) (supporting information Table S5). Gold and Platinum Group Elements (PGE) analyzed for a subgroup of samples are low compared to open-ocean Fe-Mn crusts (supporting information Table S6). Au, 3–4 ppb, is lower than typically found in crusts and nodules, which range from 3.0 to 100 ppb. Pt is the highest among the PGE for Arctic crusts, with concentrations of 78–163 ppb, compared to 470 and 567 ppb means for the Prime Crust Zone (PCZ) in the Pacific Ocean and the Atlantic crusts respectively (Hein & Koschinsky, 2014).

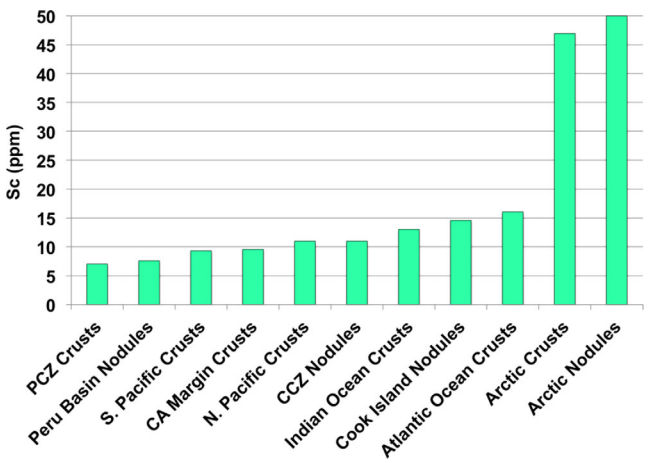

Figure 4. Mean scandium contents of Arctic Ocean Fe-Mn crusts and nodules compared to mean contents for Fe-Mn crusts and nodules from elsewhere in the global ocean; PCZ = Prime Crust Zone in the Pacific, CA = California, CCZ = Clarion-Clipperton Zone; data from Hein et al. (2013a) and Hein et al. (2015).

Si/Al ratios vary from 0.67 to 4.79 (mean 1.75) for the entire data set, 1.03–2.62 (mean 1.75) for bulk crusts, and 1.37–2.05 (mean 1.64) for nodules. The two highest ratios (outliers), 4.79 and 3.80, are found in the outermost 4 mm thick layer of crusts DR5-D-D and DR2-001D. The range encompassing continuous Si/Al ratios is 0.67–2.68, mean1.70. Samples from dredge haul DR3 (shallowest water site, 1,605 m) have the lowest Si/Al ratios, mean 1.14 (n = 7). These low mean Si/Al ratios are atypical for Fe-Mn crusts and nodules found elsewhere, which range from 2.37 to 6.09 for crusts and 2.78 to 3.43 for nodules (Hein et al., 2013a); and are much lower than ratios for many common rocks that make up the earth's crust, such as shale (2.94 PAAS) (Taylor & McLennan, 1985), MORB (2.01–2.10) (Gale et al., 2013), and continental crust (3.37) (Rudnick & Gao, 2003). This detritus in the crusts, with high Al relative to Si, requires mafic/ultramafic or Al-rich metamorphic source rocks.

TOC was measured on three layers from each of two crusts, and on four bulk crusts (supporting information Table S7). TOC contents are generally low, and vary by a factor of 2.4, from 0.124% to 0.293%. TOC increases progressively from the lower layer to the top layer of both crusts analyzed. This can be attributed to increasing productivity with

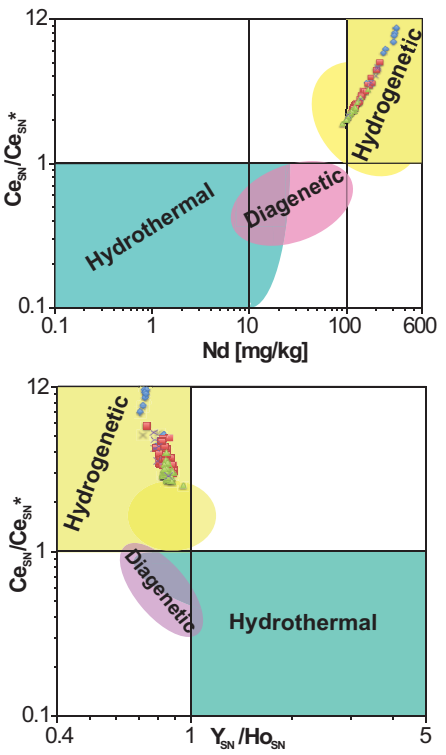

Figure 5. Genetic discrimination plots for Fe-Mn crusts and nodules, after Bau et al. (2014), showing a hydrogenetic origin for the Arctic Ocean crusts and nodules; Co is a good indicator of hydrogenesis and reflects the Mn-oxide phases; for crusts: blue diamonds Co > 2,000 ppm, red squares Co 1,000–2,000 ppm, and green triangles Co < 1,000 ppm, x = nodules with Co contents of 893–1,884 ppm.

time, or to loss of organic carbon with time, perhaps through diagenesis. Since TOC content generally increases with decreasing water depth, control by primary productivity seems to be the dominant process. $CaCO_3$ in these same samples is generally very low (supporting information Table S7), indicating low contents of biogenic calcite and aragonite as well as low detrital carbonate minerals. The two crusts with layers analyzed show the highest $CaCO_3$ in the uppermost layer.

3.2.1. Rare Earth Elements Plus Yttrium

Total REY for the bulk crusts vary from 0.102% to 0.370%, mean 0.165% ($\sum$REY in supporting information Table S2) and for nodules from 0.106% to 0.196%, mean 0.149%. This mean for the crusts is lower than those for crusts from elsewhere in the global ocean (0.235%–0.254%), except for the south Pacific (0.163%) (Hein et al., 2013a). The percent Heavy REY (HREY; Eu-Lu + Y; supporting information Table S2) complement of the total REY in bulk crusts varies from 17% to 27%, mean 23%, and in contrast, is generally higher than for crusts from elsewhere in the global ocean (16%–21%) (Hein et al., 2013a).

PAAS-normalized REY plots, with Y placed between Dy and Ho based on ionic radius, show typical hydrogenetic Fe-Mn crust patterns, with positive Ce anomalies, negative Y anomalies, and slight HREE enrichment, although the middle (MREE) and HREE show nearly flat patterns (supporting information Figure S1). Nodules show the same Ce and Y anomalies but MREE enrichment shows a convex up pattern (supporting information Figure S1).

REY-based discrimination plots (Bau et al., 2014) show that the Fe-Mn crusts plot in the hydrogenetic field (Figure 5). The data trend toward the diagenetic field with decreasing Co and Mn contents, and nodule data points overlap with crust data with moderate and low Co contents.

3.2.2. Scandium

Mean and maximum Sc contents for all bulk crusts from each dredge do not show a regional distribution pattern with latitude, longitude, or water depth (supporting information Figures S2 and S3). When all data are plotted against water depth, the range of values for samples from each dredge generally overlap at the various water depths (supporting information Figure S3). This is in contrast to data for crusts from a Pacific seamount where Sc content in the surface layer of crusts increased with increasing water depth (Nozaki et al., 2016); Sc in those samples correlated with Fe.

Because high Sc concentrations are unique to Arctic Ocean Fe-Mn crusts and nodules (Figure 4), we looked for clues to its origin using SEM-EDX and microprobe. SEM-EDX element maps showed elevated Sc levels uniformly distributed through the oxide matrix; high Sc contents were also identified in several types of detrital minerals and biogenic debris (Figure 6).

Microprobe line scans through polished thin sections of two crusts, DS2–008A and DS2–006G (Figures 7a and 7b), recorded Sc concentration data for 223 and 245 profile spot analyses, respectively. Both crusts showed similar results, with DS2–008A averaging 39 ppm Sc content for the Fe-Mn matrix and 40 ppm for the detrital grains, compared to 41 ppm Sc for the bulk crust determined by ICP-MS analysis; DS2–006G averaged 41 ppm Sc content for the Fe-Mn matrix and 38 ppm for the detrital grains, compared to 39 ppm Sc for the bulk crust from ICP-MS. Mass balance calculations for DS2–008A show about 65% oxide matrix and 35% detrital material.

3.2.3. Temporal Variations

Four layers were analyzed from crust DR2-001D, with Mn, Co, and Ni showing progressively higher concentrations with time (from the lowermost oldest layer to uppermost youngest layer), as do Ca, Bi, Pb, Se, Te, Th, Tl, La, Pr, Nd, and Sm. Elements with higher concentrations in the older layer (Al, K, Cs, Ga, Li, Sc) progressively decrease with time (supporting information Table S5). All other elements show the

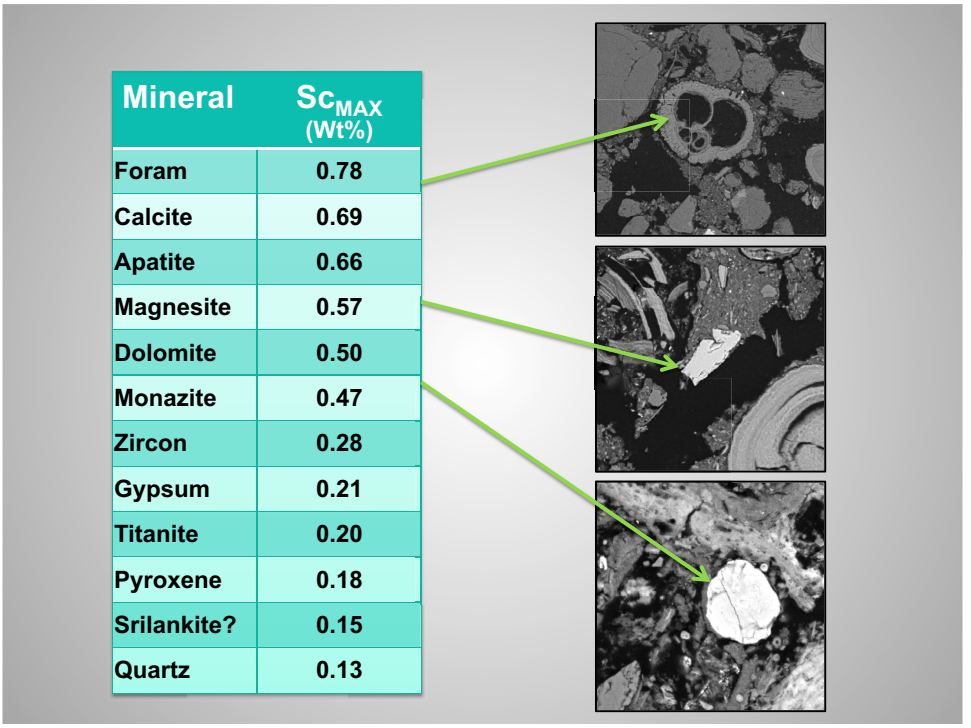

Figure 6. SEM photomicrographs and examples of some of the many different types of detrital minerals in the Fe-Mn crusts, and the maximum Sc content in each grain type shown; foram = foraminifera test (calcite).

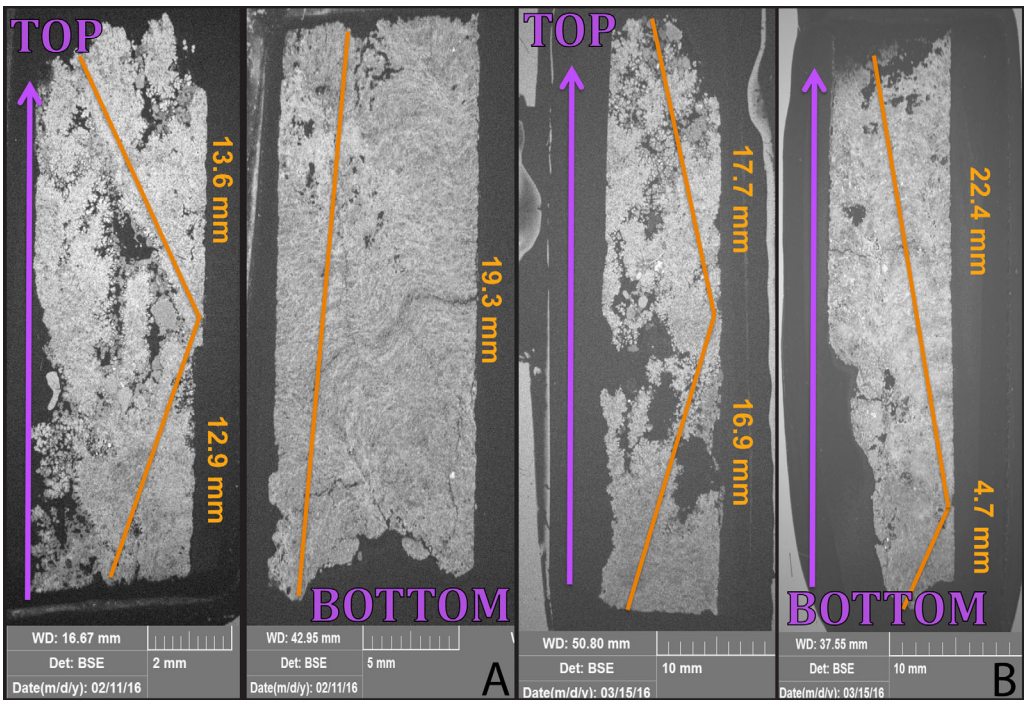

Figure 7. SEM photomicrographs of polished thin sections through two crusts showing (a) Microprobe scan line (orange) of crust DS2–008A (top and bottom, left two panel) along which 223 Sc spot analyses were made, and (b) microprobe scan line (orange) of crust DS2–006G (top and bottom, right two panel) along which 245 Sc spot analyses were made. Scan lines placed to avoid large-scale porosity.

Table 3
Correlation Coefficient Matrix for Combined Sample Geochemical Data Set

	Growth rate	Fe	Mn	Si	Al	Ca	Mg	Na	K	Ti	P	As	Ba
Growth rate	**1.000**												
Fe	**0.347**	**1.000**											
Mn	**−0.707**	0.080	**1.000**										
Si	0.187	**−0.727**	**−0.681**	**1.000**									
Al	**0.756**	0.124	**−0.902**	**0.453**	**1.000**								
Ca	**−0.748**	−0.150	**0.924**	**−0.449**	**−0.952**	**1.000**							
Mg	**−0.484**	0.119	**0.729**	**−0.511**	**−0.765**	**0.787**	**1.000**						
Na	0.215	−0.033	**−0.324**	0.122	**0.300**	**−0.321**	−0.229	**1.000**					
K	**0.596**	−0.212	**−0.894**	**0.717**	**0.889**	**−0.866**	**−0.760**	0.219	**1.000**				
Ti	−0.025	−0.094	−0.185	0.196	0.155	−0.095	0.040	0.155	0.201	**1.000**			
P	**0.624**	**0.873**	−0.235	**−0.476**	**0.427**	**−0.417**	−0.115	0.123	0.054	−0.101	**1.000**		
As	0.006	**0.686**	**0.341**	**−0.779**	−0.206	0.137	0.235	−0.040	**−0.433**	−0.142	**0.474**	**1.000**	
Ba	**−0.409**	**0.286**	**0.774**	**−0.682**	**−0.630**	**0.620**	**0.496**	**−0.314**	**−0.606**	−0.060	−0.008	**0.479**	**1.000**
Be	−0.031	**0.471**	**0.275**	**−0.634**	−0.068	0.050	−0.015	0.031	**−0.277**	−0.118	**0.346**	**0.813**	**0.505**
Bi	**−0.664**	0.091	**0.855**	**−0.542**	**−0.886**	**0.862**	**0.816**	**−0.322**	**−0.817**	−0.014	−0.261	**0.373**	**0.714**
Cd	**−0.485**	**0.296**	**0.864**	**−0.776**	**−0.686**	**0.762**	**0.714**	−0.179	**−0.824**	−0.133	0.086	**0.427**	**0.746**
Co	**−0.734**	−0.067	**0.919**	**−0.529**	**−0.935**	**0.944**	**0.777**	**−0.306**	**−0.869**	−0.074	**−0.388**	**0.331**	**0.678**
Cr	**0.319**	−0.260	**−0.664**	**0.596**	**0.526**	**−0.558**	**−0.517**	0.105	**0.592**	0.255	−0.077	**−0.292**	**−0.667**
Cu	**−0.541**	−0.047	**0.507**	**−0.300**	**−0.515**	**0.472**	**0.463**	−0.105	**−0.502**	−0.029	−0.159	0.011	0.202
Li	**0.624**	0.142	**−0.630**	0.171	**0.750**	**−0.707**	**−0.462**	**0.367**	**0.537**	0.003	**0.487**	0.008	**−0.507**
Mo	**−0.402**	**0.365**	**0.790**	**−0.834**	**−0.616**	**0.632**	**0.477**	−0.115	**−0.756**	−0.202	0.107	**0.693**	**0.736**
Nb	**−0.502**	0.253	**0.780**	**−0.640**	**−0.771**	**0.726**	**0.805**	**−0.349**	**−0.766**	0.024	−0.059	**0.428**	**0.759**
Ni	**−0.687**	0.018	**0.944**	**−0.601**	**−0.900**	**0.893**	**0.748**	**−0.342**	**−0.840**	−0.185	**−0.323**	**0.380**	**0.725**
Pb	**−0.644**	0.113	**0.893**	**−0.632**	**−0.912**	**0.880**	**0.794**	**−0.296**	**−0.877**	−0.035	−0.224	**0.458**	**0.773**
Rb	**0.496**	−0.211	**−0.831**	**0.668**	**0.855**	**−0.820**	**−0.742**	0.229	**0.964**	**0.277**	0.006	**−0.373**	**−0.549**
S	**−0.385**	**0.366**	**0.744**	**−0.753**	**−0.618**	**0.652**	**0.672**	−0.015	**−0.776**	−0.075	0.201	**0.341**	**0.684**
Sb	**−0.395**	0.175	**0.526**	**−0.396**	**−0.492**	**0.531**	**0.568**	−0.166	**−0.510**	0.132	0.092	0.021	**0.481**
Sc	**0.455**	**0.634**	−0.253	**−0.304**	**0.447**	**−0.419**	−0.229	0.174	0.211	−0.003	**0.652**	**0.526**	−0.017
Sr	**−0.517**	**0.307**	**0.928**	**−0.803**	**−0.808**	**0.816**	**0.673**	**−0.307**	**−0.866**	−0.156	0.007	**0.517**	**0.901**
Th	**−0.582**	0.188	**0.838**	**−0.662**	**−0.824**	**0.821**	**0.799**	−0.197	**−0.844**	−0.008	−0.094	**0.474**	**0.717**
Tl	**−0.692**	−0.025	**0.825**	**−0.538**	**−0.755**	**0.786**	**0.578**	−0.211	**−0.733**	−0.183	**−0.290**	**0.300**	**0.574**
U	**−0.572**	0.191	**0.849**	**−0.666**	**−0.658**	**0.746**	**0.582**	−0.264	**−0.737**	−0.154	−0.050	**0.373**	**0.605**
V	−0.099	**0.687**	**0.404**	**−0.736**	**−0.337**	0.237	**0.370**	−0.170	**−0.520**	−0.068	**0.439**	**0.535**	**0.473**
W	**−0.359**	**0.395**	**0.761**	**−0.846**	**−0.586**	**0.586**	**0.456**	−0.142	**−0.718**	−0.184	0.111	**0.754**	**0.754**
Zn	**−0.326**	**0.450**	**0.695**	**−0.760**	**−0.548**	**0.547**	**0.575**	−0.215	**−0.707**	−0.130	**0.300**	**0.333**	**0.662**
Zr	**−0.329**	−0.253	**0.358**	−0.023	**−0.483**	**0.500**	**0.280**	−0.033	**−0.412**	−0.167	**−0.327**	−0.030	0.042
La	**−0.462**	**0.323**	**0.889**	**−0.797**	**−0.786**	**0.786**	**0.671**	**−0.282**	**−0.826**	−0.129	−0.006	**0.588**	**0.888**
Ce	**−0.510**	**0.391**	**0.872**	**−0.848**	**−0.740**	**0.743**	**0.628**	−0.219	**−0.834**	−0.091	0.043	**0.650**	**0.841**
Pr	**−0.454**	**0.333**	**0.884**	**−0.805**	**−0.774**	**0.772**	**0.656**	**−0.283**	**−0.822**	−0.136	0.003	**0.598**	**0.884**
Nd	**−0.454**	**0.341**	**0.883**	**−0.810**	**−0.771**	**0.770**	**0.654**	**−0.282**	**−0.824**	−0.140	0.010	**0.599**	**0.884**
Sm	**−0.456**	**0.348**	**0.885**	**−0.820**	**−0.766**	**0.764**	**0.655**	**−0.282**	**−0.826**	−0.128	0.020	**0.613**	**0.886**
Eu	**−0.448**	**0.372**	**0.884**	**−0.832**	**−0.749**	**0.758**	**0.654**	**−0.276**	**−0.826**	−0.137	0.061	**0.596**	**0.890**
Gd	**−0.473**	**0.368**	**0.899**	**−0.834**	**−0.770**	**0.777**	**0.670**	**−0.274**	**−0.846**	−0.137	0.052	**0.598**	**0.887**
Tb	**−0.506**	**0.350**	**0.908**	**−0.834**	**−0.782**	**0.788**	**0.681**	−0.268	**−0.856**	−0.128	0.029	**0.612**	**0.876**
Dy	**−0.516**	**0.351**	**0.918**	**−0.838**	**−0.792**	**0.801**	**0.694**	−0.270	**−0.872**	−0.124	0.043	**0.578**	**0.872**
Y	**−0.519**	**0.361**	**0.916**	**−0.835**	**−0.778**	**0.799**	**0.701**	−0.261	**−0.866**	−0.129	0.058	**0.554**	**0.858**
Ho	**−0.512**	**0.356**	**0.921**	**−0.838**	**−0.787**	**0.805**	**0.702**	−0.265	**−0.874**	−0.129	0.057	**0.557**	**0.871**
Er	**−0.529**	**0.339**	**0.921**	**−0.823**	**−0.797**	**0.814**	**0.714**	−0.270	**−0.878**	−0.116	0.052	**0.514**	**0.859**
Tm	**−0.582**	**0.277**	**0.936**	**−0.789**	**−0.844**	**0.847**	**0.724**	**−0.305**	**−0.897**	−0.170	−0.038	**0.530**	**0.813**
Yb	**−0.531**	**0.349**	**0.920**	**−0.819**	**−0.796**	**0.819**	**0.725**	−0.270	**−0.880**	−0.134	0.060	**0.505**	**0.847**
Lu	**−0.538**	**0.338**	**0.925**	**−0.830**	**−0.802**	**0.820**	**0.722**	−0.256	**−0.897**	−0.145	0.063	**0.516**	**0.831**

	Be	Bi	Cd	Co	Cr	Cu	Li	Mo	Nb	Ni	Pb	Rb
Be	**1.000**											
Bi	0.173	**1.000**										
Cd	**0.419**	**0.716**	**1.000**									
Co	0.213	**0.921**	**0.759**	**1.000**								
Cr	−0.232	**−0.584**	**−0.717**	**−0.559**	**1.000**							
Cu	−0.063	**0.366**	**0.390**	**0.402**	−0.185	**1.000**						

Table 3. *(continued)*

	Be	Bi	Cd	Co	Cr	Cu	Li	Mo	Nb	Ni	Pb	Rb
Li	0.131	**−0.711**	**−0.334**	**−0.684**	**0.293**	−0.174	**1.000**					
Mo	**0.676**	**0.601**	**0.812**	**0.696**	**−0.619**	0.258	**−0.291**	**1.000**				
Nb	0.211	**0.881**	**0.735**	**0.804**	**−0.561**	**0.352**	**−0.556**	**0.569**	**1.000**			
Ni	0.238	**0.881**	**0.769**	**0.921**	**−0.617**	**0.437**	**−0.651**	**0.729**	**0.790**	**1.000**		
Pb	**0.291**	**0.962**	**0.770**	**0.951**	**−0.606**	**0.401**	**−0.654**	**0.726**	**0.887**	**0.896**	**1.000**	
Rb	−0.204	**−0.750**	**−0.765**	**−0.808**	**0.552**	**−0.460**	**0.506**	**−0.674**	**−0.723**	**−0.772**	**−0.815**	**1.000**
S	**0.294**	**0.631**	**0.832**	**0.620**	**−0.684**	**0.406**	**−0.319**	**0.667**	**0.699**	**0.615**	**0.688**	**−0.741**
Sb	−0.053	**0.501**	**0.564**	**0.425**	**−0.379**	**0.420**	**−0.428**	**0.293**	**0.554**	**0.405**	**0.478**	**−0.500**
Sc	**0.473**	−0.249	−0.027	**−0.343**	0.107	**−0.421**	**0.315**	0.136	−0.170	−0.261	−0.269	0.236
Sr	**0.469**	**0.814**	**0.887**	**0.837**	**−0.686**	**0.338**	**−0.564**	**0.861**	**0.809**	**0.854**	**0.884**	**−0.816**
Th	**0.289**	**0.921**	**0.806**	**0.896**	**−0.644**	**0.387**	**−0.514**	**0.718**	**0.864**	**0.812**	**0.947**	**−0.771**
Tl	**0.311**	**0.661**	**0.722**	**0.767**	**−0.541**	**0.463**	**−0.466**	**0.795**	**0.525**	**0.799**	**0.728**	**−0.654**
U	**0.317**	**0.692**	**0.783**	**0.737**	**−0.549**	**0.364**	**−0.500**	**0.726**	**0.576**	**0.783**	**0.688**	**−0.644**
V	**0.356**	**0.335**	**0.419**	**0.279**	−0.259	**0.398**	−0.230	**0.511**	**0.489**	**0.325**	**0.428**	**−0.515**
W	**0.722**	**0.589**	**0.763**	**0.678**	**−0.560**	0.201	**−0.299**	**0.961**	**0.589**	**0.720**	**0.710**	**−0.634**
Zn	**0.286**	**0.509**	**0.749**	**0.496**	**−0.574**	**0.551**	−0.224	**0.622**	**0.631**	**0.555**	**0.586**	**−0.702**
Zr	−0.147	**0.338**	0.191	**0.481**	−0.103	0.245	**−0.327**	0.216	0.157	**0.343**	**0.388**	**−0.442**
La	**0.492**	**0.821**	**0.841**	**0.840**	**−0.658**	0.242	**−0.580**	**0.865**	**0.806**	**0.853**	**0.889**	**−0.771**
Ce	**0.564**	**0.804**	**0.849**	**0.826**	**−0.663**	**0.293**	**−0.524**	**0.900**	**0.788**	**0.816**	**0.873**	**−0.749**
Pr	**0.512**	**0.805**	**0.839**	**0.827**	**−0.660**	0.229	**−0.573**	**0.878**	**0.794**	**0.854**	**0.876**	**−0.766**
Nd	**0.515**	**0.801**	**0.841**	**0.823**	**−0.660**	0.235	**−0.570**	**0.879**	**0.791**	**0.852**	**0.873**	**−0.769**
Sm	**0.528**	**0.804**	**0.845**	**0.824**	**−0.656**	0.246	**−0.558**	**0.873**	**0.803**	**0.853**	**0.873**	**−0.769**
Eu	**0.524**	**0.786**	**0.868**	**0.802**	**−0.670**	0.239	**−0.536**	**0.874**	**0.791**	**0.828**	**0.854**	**−0.772**
Gd	**0.513**	**0.817**	**0.877**	**0.828**	**−0.684**	**0.273**	**−0.551**	**0.865**	**0.812**	**0.845**	**0.878**	**−0.791**
Tb	**0.522**	**0.827**	**0.877**	**0.843**	**−0.669**	**0.300**	**−0.548**	**0.882**	**0.810**	**0.859**	**0.889**	**−0.791**
Dy	**0.487**	**0.825**	**0.891**	**0.844**	**−0.680**	**0.345**	**−0.554**	**0.867**	**0.819**	**0.847**	**0.891**	**−0.813**
Y	**0.466**	**0.816**	**0.907**	**0.825**	**−0.692**	**0.351**	**−0.552**	**0.855**	**0.811**	**0.849**	**0.866**	**−0.804**
Ho	**0.473**	**0.829**	**0.906**	**0.840**	**−0.695**	**0.354**	**−0.539**	**0.851**	**0.825**	**0.845**	**0.887**	**−0.816**
Er	**0.432**	**0.823**	**0.904**	**0.835**	**−0.677**	**0.398**	**−0.550**	**0.823**	**0.829**	**0.832**	**0.881**	**−0.825**
Tm	**0.421**	**0.841**	**0.872**	**0.870**	**−0.627**	**0.415**	**−0.603**	**0.834**	**0.810**	**0.879**	**0.890**	**−0.846**
Yb	**0.411**	**0.826**	**0.910**	**0.830**	**−0.688**	**0.394**	**−0.557**	**0.813**	**0.818**	**0.838**	**0.872**	**−0.831**
Lu	**0.427**	**0.806**	**0.911**	**0.829**	**−0.673**	**0.440**	**−0.527**	**0.833**	**0.808**	**0.842**	**0.870**	**−0.850**

	S	Sb	Sc	Sr	Th	Tl	U	V	W	Zn	Zr	La	Ce
S	**1.000**												
Sb	**0.692**	**1.000**											
Sc	−0.069	−0.050	**1.000**										
Sr	**0.812**	**0.553**	−0.054	**1.000**									
Th	**0.749**	**0.542**	−0.175	**0.839**	**1.000**								
Tl	**0.568**	**0.367**	−0.246	**0.733**	**0.673**	**1.000**							
U	**0.694**	**0.557**	0.050	**0.783**	**0.702**	**0.754**	**1.000**						
V	**0.544**	**0.385**	0.159	**0.542**	**0.405**	**0.301**	**0.281**	**1.000**					
W	**0.611**	0.244	0.221	**0.855**	**0.681**	**0.686**	**0.682**	**0.533**	**1.000**				
Zn	**0.851**	**0.698**	−0.074	**0.763**	**0.608**	**0.546**	**0.595**	**0.691**	**0.570**	**1.000**			
Zr	0.059	0.016	**−0.375**	0.218	**0.371**	**0.346**	0.194	−0.026	0.139	0.043	**1.000**		
La	**0.735**	**0.462**	0.016	**0.975**	**0.835**	**0.693**	**0.739**	**0.526**	**0.892**	**0.658**	0.225	**1.000**	
Ce	**0.753**	**0.445**	0.041	**0.942**	**0.854**	**0.732**	**0.765**	**0.566**	**0.902**	**0.659**	0.230	**0.955**	**1.000**
Pr	**0.730**	**0.448**	0.029	**0.973**	**0.816**	**0.706**	**0.742**	**0.531**	**0.903**	**0.660**	0.200	**0.998**	**0.955**
Nd	**0.735**	**0.457**	0.034	**0.973**	**0.813**	**0.709**	**0.745**	**0.540**	**0.904**	**0.668**	0.196	**0.997**	**0.955**
Sm	**0.740**	**0.469**	0.047	**0.974**	**0.820**	**0.685**	**0.751**	**0.541**	**0.907**	**0.675**	0.183	**0.995**	**0.956**
Eu	**0.773**	**0.515**	0.078	**0.980**	**0.814**	**0.683**	**0.764**	**0.543**	**0.898**	**0.714**	0.162	**0.988**	**0.947**
Gd	**0.780**	**0.520**	0.050	**0.983**	**0.844**	**0.682**	**0.775**	**0.539**	**0.884**	**0.708**	0.197	**0.989**	**0.956**
Tb	**0.779**	**0.523**	0.048	**0.980**	**0.858**	**0.711**	**0.796**	**0.535**	**0.899**	**0.706**	0.209	**0.985**	**0.962**
Dy	**0.817**	**0.570**	0.003	**0.984**	**0.867**	**0.709**	**0.800**	**0.556**	**0.873**	**0.747**	0.222	**0.976**	**0.959**
Y	**0.830**	**0.618**	0.050	**0.975**	**0.853**	**0.710**	**0.837**	**0.543**	**0.855**	**0.757**	0.189	**0.960**	**0.946**
Ho	**0.833**	**0.592**	0.000	**0.984**	**0.873**	**0.701**	**0.809**	**0.539**	**0.852**	**0.762**	0.226	**0.968**	**0.954**
Er	**0.850**	**0.640**	−0.028	**0.978**	**0.872**	**0.686**	**0.805**	**0.553**	**0.821**	**0.787**	0.238	**0.951**	**0.936**
Tm	**0.766**	**0.583**	−0.016	**0.961**	**0.849**	**0.740**	**0.816**	**0.532**	**0.842**	**0.709**	0.269	**0.950**	**0.926**

Table 3. *(continued)*

	S	Sb	Sc	Sr	Th	Tl	U	V	W	Zn	Zr	La	Ce
Yb	**0.844**	**0.648**	−0.011	**0.972**	**0.861**	**0.702**	**0.814**	**0.542**	**0.806**	**0.788**	0.240	**0.944**	**0.924**
Lu	**0.854**	**0.645**	−0.033	**0.969**	**0.854**	**0.727**	**0.815**	**0.566**	**0.819**	**0.808**	0.254	**0.934**	**0.921**

	Pr	Nd	Sm	Eu	Gd	Tb	Dy	Y	Ho	Er	Tm	Yb	Lu
Pr	**1.000**												
Nd	**0.999**	**1.000**											
Sm	**0.996**	**0.997**	**1.000**										
Eu	**0.988**	**0.989**	**0.991**	**1.000**									
Gd	**0.986**	**0.986**	**0.991**	**0.995**	**1.000**								
Tb	**0.983**	**0.984**	**0.989**	**0.992**	**0.995**	**1.000**							
Dy	**0.972**	**0.972**	**0.978**	**0.985**	**0.992**	**0.994**	**1.000**						
Y	**0.957**	**0.960**	**0.967**	**0.976**	**0.983**	**0.985**	**0.988**	**1.000**					
Ho	**0.962**	**0.963**	**0.970**	**0.979**	**0.989**	**0.989**	**0.996**	**0.991**	**1.000**				
Er	**0.943**	**0.945**	**0.954**	**0.965**	**0.977**	**0.976**	**0.989**	**0.987**	**0.995**	**1.000**			
Tm	**0.945**	**0.947**	**0.953**	**0.956**	**0.967**	**0.974**	**0.975**	**0.977**	**0.973**	**0.970**	**1.000**		
Yb	**0.935**	**0.938**	**0.944**	**0.962**	**0.973**	**0.972**	**0.985**	**0.985**	**0.991**	**0.992**	**0.974**	**1.000**	
Lu	**0.928**	**0.932**	**0.938**	**0.954**	**0.964**	**0.968**	**0.981**	**0.982**	**0.986**	**0.989**	**0.975**	**0.993**	**1.000**

Note. Bolded correlations at 99% confidence level.

highest concentrations in one of the middle two layers or show little variation through the four crust layers.

Three layers were analyzed in five Fe-Mn crusts and the elements that progressively increase with time in all five crusts are: Bi, Nb, Ni, Pb, Ta, and La and in four of the five crusts: Ca, Sb, Se, Te, Th, Tl, Zr, Pr, Nd, and Tm. Those that decrease progressively with time in all five crusts are Al and Li, and K and Rb decreased in four of five crusts (supporting information Table S5). Mn and Co increase with time in three of the crusts (Mn-oxide phases) and Fe, P, As, Hf, and Sc decrease with time in two crusts (Fe-oxyhydroxide phases).

3.2.4. Element Correlations

A correlation coefficients matrix was generated for each of the four sample groups, and elements with correlations with >99% CL were determined and are listed for the combined data set (Table 3). Based on the correlation coefficients and the XRD mineralogy, three phases are listed with decreasing coefficient values for each phase:

1. *Mn-phases*: Mn, Ni, Ca, Sr, Co, each REY, Pb, Cd, Bi, U, Th, Tl, Mo, Nb, Ba, W, S, Mg, Zn, Sb, Cu, V, Zr, As, and Be;
2. *Fe-phases*: Fe, P, V, As, Sc, Be, Zn, W, the REY, S, Mo, Sr, Cd, and Ba;
3. *Detrital phase* (correlations with Si and Al): Al, Si, K, Rb, and Cr; Li, Sc, and Na correlate with Al but not with Si.

The correlation coefficients for the REY are much stronger for the Mn phases than for the Fe phases.

A large number of elements show correlations with water depth. Elements that decrease in Fe-Mn crusts with increasing water depth (inverse correlations at 99% CL) are the REY, Sr, Ba, S, Cd, Th, Sb, Ca, Bi, Te, Pb, Nb, Mn, Co, Mg Ni, U, Zn, W, and Mo, with Tl and Fe showing negative correlations at the 95% CL. Elements that define the detrital phase increase in crusts with increasing water depth, Al, Li, Cr, Rb, K, and Si. Sc, P, and Na do not correlate with water depth.

3.2.5. Q-Mode Factor Analyses

Four Q-mode factors for the combined data set account for 95% of the variance in the data, with all communalities ≥0.9. Factor 1 is interpreted to be the aluminosilicate detrital phase and accounts for most of the variance, 52%, with Factor 2, the Mn-phases accounting for 34%, Factor 3, the Fe-phases, 7%, and Factor 4, a phase interpreted as a residual biogenic phase accounts for 2% of the variance. The elements with the highest rotated factor scores (see Figure 8 for all elements) for each factor are—*Detrital*: Al, K, Rb, Sc, Fe, P, Si, Be, Cr, Li, and As; *Mn-phases*: S, Zn, REY, U, Ca, Sr, Mn, Co, Ni, Sb, Th, V, and Cd; *Fe-phases*: P, Fe, As, V, Be, and Sc; and the *residual biogenic*: Sb, Zn, S, Cu, V, P, Mg, and Fe.

Two major differences are noted when compared to the Pearson correlations associated with each phase (Figure 8 and Table 3). First, a residual biogenic phase was identified using Q-mode analysis, which is a common component of Fe-Mn crusts collected elsewhere in the global ocean (Hein et al., 2000); and second, the larger number of elements in the detrital phase, Factor 1, compared to the smaller number of elements

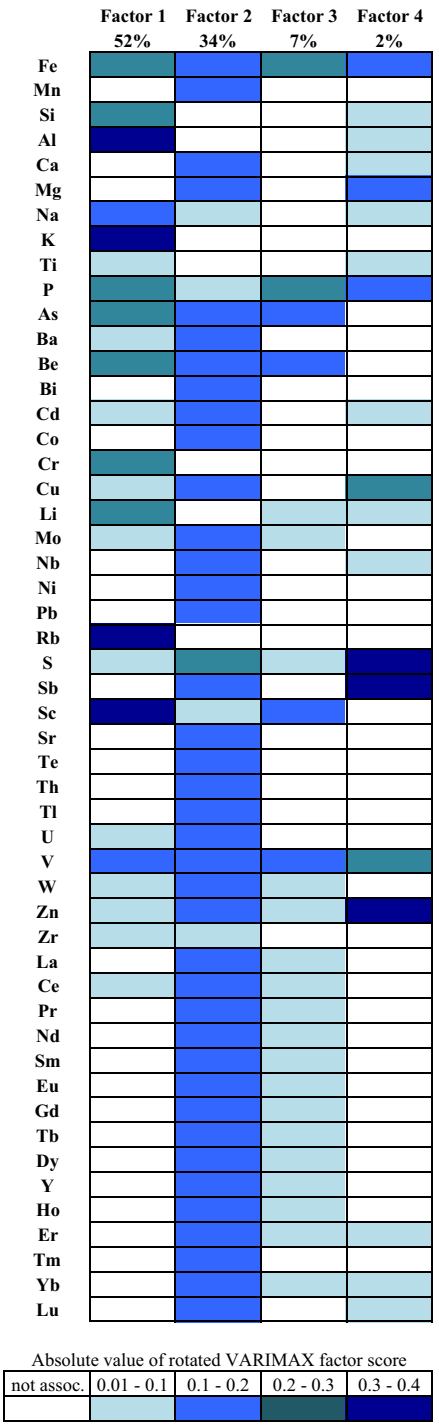

Figure 8. Q-mode factor analysis for the combined data set; all communalities are ≥0.9.

that correlate with Al and Si. Factor 1 associated elements better reflect the minor minerals associated with the detritus and possible significant correlations that occur below the 99% CL.

A comparison between Fe and Sc is interesting because they have previously been shown to behave similarly in several ways: There is evidence that Sc and Fe have similar inorganic speciation in the ocean as $M(OH)_3$ (Byrne, 2002) and also that Sc may be able to substitute for Fe in organic Fe-binding complexes (Rogers et al., 1980). Parker et al. (2016) suggested that it may be possible to use the similarities and differences between these two elements to tease apart the many facets of the oceanic Fe cycle. The question has been, in what ways precisely do the reactivities of Fe and Sc differ? Our statistical relations show that Sc is dominantly associated with FeO(OH) and to a lesser extent with detrital minerals. Interestingly, it appears that while both Fe and Sc are a part of detritus in minerals such as amphiboles and pyroxenes, Sc is also in many other detrital minerals that do not contain Fe such as apatite and calcite. Identifying differences like this between the oceanic cycling of Fe and Sc is an important step toward being able to actually use Sc to elucidate the Fe cycle, rather than to simply theorize about it.

3.3. Growth Rates and Ages

The age of initiation of Fe-Mn crust growth varies from 14.8 to 0.7 Myr ago based on the Manheim and Lane-Bostwick (1988) Co chronometer. The ages of three crusts (DS1-001, DS2–006G, and DS4–006B) dated using Be isotopes (8.13–6.21 Myr) (Dausmann et al., 2015) fall within the range determined using the Co chronometer. The Co chronometer cannot detect hiatuses in a crust, but the crusts analyzed using Be isotopes can, but did not show growth hiatuses. However, the dates of initiation of crust growth calculated here should be viewed with this caveat in mind.

Growth rates for Arctic bulk crusts vary from 2.23 to 23.3 mm/Myr for the crusts and nodules, and for crust layers from 1.1 to 42.1 mm/Myr (Figure 9 and supporting information Table S8). Growth rates for three crusts that vary from 2.18 to 26.7 mm/Myr were determined using Be isotopes (Dausmann et al., 2015). Growth rates decreased with time in all crust samples where two or more layers were analyzed, except for one crust (DS1–010B) with three layers where the middle layer had the fastest growth rate. Growth rates typical of hydrogenetic Fe-Mn crusts formed elsewhere in the global ocean vary from 1 to 5 mm/Myr for 75% of samples analyzed; growth rates greater than about 10 mm/Myr are usually considered to have a hydrothermal input (e.g., Hein et al., 2000), however hydrothermal fields have not existed in the Amerasia Arctic during the growth history of the Fe-Mn crusts. Of the calculated growth rates for Arctic crusts, 33% are atypical (≥11 mm/Myr) compared to most other hydrogenetic crusts.

Growth rate values show a positive correlation (99% CL) with Al, P, Li, K, Rb, Sc, and Cr, negative correlations with Ca, Co, Tl, Ni, Bi, and Pb, and no correlation with Si. We interpret this to mean that growth rates increase with increasing amounts of Al-rich detritus. Growth rates are also assumed to increase with increasing Fe-oxyhydroxide minerals and slower growth rates with increasing Mn-oxide minerals, as Fe and Mn contents are part of the equation used to calculate growth rates; this idea is supported by the limited isotope-determined growth-rate data. The correlations listed with growth rates are only valid for elements that do not correlate with Fe or Mn: Al, Li, K, and Rb.

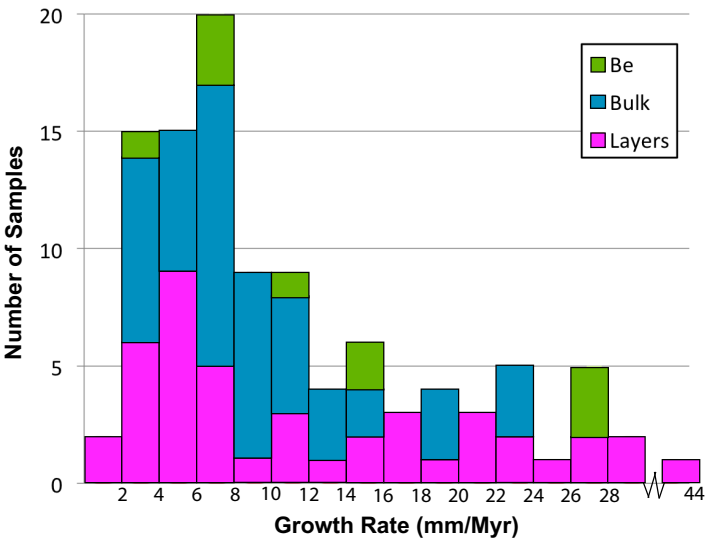

Figure 9. Histogram of growth rates of Arctic Ocean crusts and nodules; Be growth rates determined using Be isotopes, all others calculated using the Manheim and Lane-Bostwick (1988) equation.

3.4. Seawater Scandium Profiles

Dissolved Sc (dSc) and particulate Sc (pSc) concentrations were measured in samples from seawater profiles in the Arctic Ocean. Data for four full-water-depth profiles (stations 19, 48, 52, and 57; Figure 2) are discussed here. For comparison, data are presented here for two dSc Pacific profiles (EPZT 5, EPZT 15) along with two published dSc (EPZT 1, Japanese) and three published pSc profiles (EPZT, 1, 5, 15) (Figure 10). EPZT profiles are from the SE Pacific off Peru, and the Japanese profile is from the North Pacific.

Profiles of dSc from the Atlantic and Pacific Oceans showed increasing concentrations with water depth (Parker et al., 2016). An example of these profiles from the GEOTRACES EPZT cruise is shown in Figure 10a. In contrast in the Arctic, the dSc profiles show a surface water minimum, a maximum at ~190 m that progressively decreases again down to ~500 m, then only gradual increases with depth to the seabed, ending in the Bottom Nepheloid Layer (BNL) with a near-bottom increase at all four sites (Figure 10a). Thus, while Arctic profiles do increase in dSc with water depth, there are two notable differences between dSc profiles in the Arctic and elsewhere in the global ocean. First, there are individual layers of increased dSc in the Arctic that can somewhat obscure the general trend of increasing dSc concentration with depth, and second, the dSc concentrations in the Arctic, especially in the enriched layers, are higher than elsewhere in the global ocean. The 190 m dSc maxima at all stations in the Arctic appear to significantly diverge from the standard oceanic dSc profile shape. This feature aligns exactly with the Arctic halocline water mass, suggesting a large dSc flux from the continental shelves, perhaps derived from margin processes and/or production of brine plumes. At the seafloor, the size of the BNL peak increases from station 57 (7 pmol/kg increase) northward to stations 52 and 48, both of which show 13 pmol/kg increases, resulting in BNL concentrations of ~25–30 pmol/kg for all sites combined; station 19 shows a smaller dSc

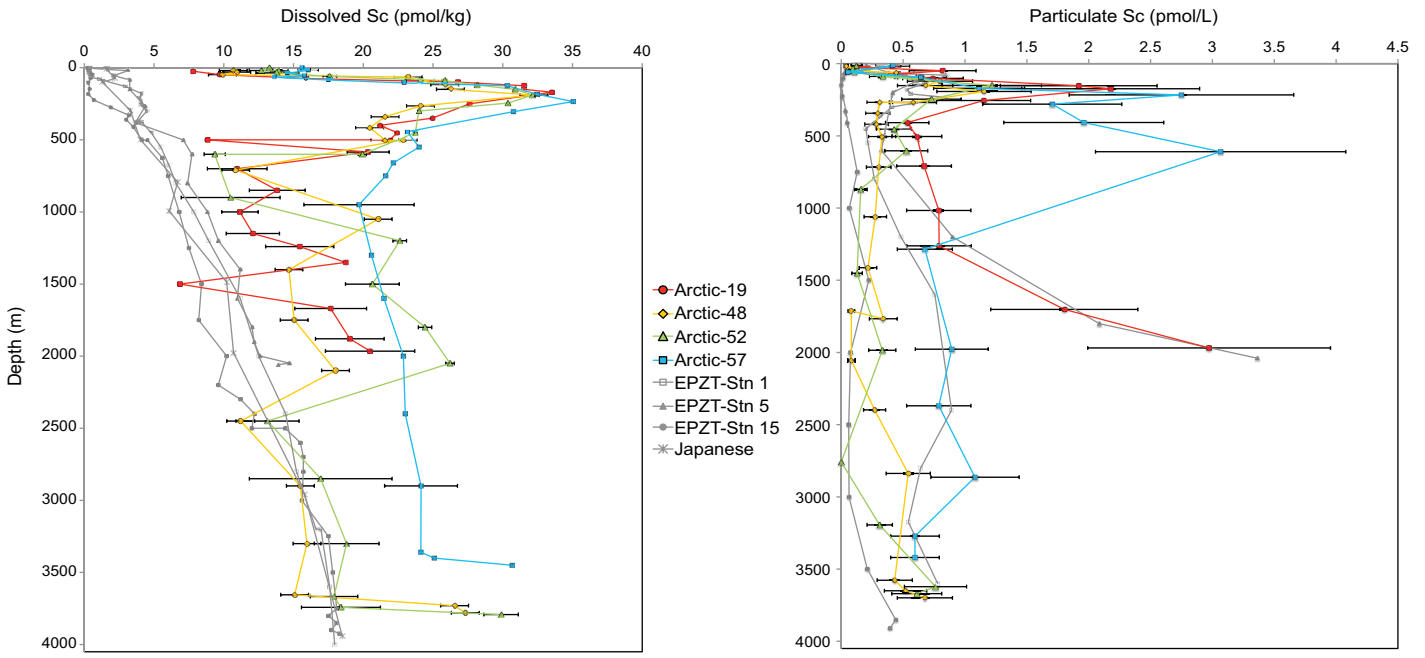

Figure 10. GEOTRACES seawater profiles for (a) dissolved Sc profiles and (b) particulate Sc profiles (SSF = small size fraction) for stations 19, 48, 52, and 57 in the Amerasia Arctic Ocean (see locations in Figure 2); EPZT = East Pacific Zonal Transect. Dissolved Sc profiles from the North Pacific Ocean (Amakawa et al., 2007) and SE Pacific (Parker et al., 2016; this study) and particulate Sc profiles from the SE Pacific (Heller et al., 2017) are shown for comparison. pSc error bars show RSD = 33%, which is a conservative estimate of uncertainty from variability in particle field, sampling, and analytical uncertainties from repeated digestions of an internal standard.

increase near the bottom compared to the other Arctic sites but was also sampled on the continental slope at a much shallower bottom depth (~2,000 m depth) compared to >3,000 m water depth for stations 48, 52, and 57. The Arctic dSc profiles from stations 19, 48, and 52 all show much more variable deep ocean dSc concentrations than in the Pacific dSc seawater profiles (Figure 10). Error bars showing the standard deviation of replicate dSc analyses for the Arctic samples suggest that the variable concentrations observed in the Arctic were reproducible features that represent a real contrast to deep water dSc from other ocean basins. Station 57 in the Arctic, the site closest to the shelf, the Chukchi Borderland, and the Mackenzie River, has higher dSc through most of the water column than at any other sites in the Arctic and elsewhere globally; yet, Arctic station 52 has higher dSc at mid-water depths than station 57 (Figure 10a). Station 57 also has the widest halocline peak at 185–550 m. Overall, major features of Arctic dSc profiles show much greater surface and halocline concentrations than in Atlantic or Pacific profiles (likely derived from transport from the margin), more variable but similar range and increasing deep-ocean concentrations in the Arctic compared to the Atlantic and Pacific, and clear BNL dSc maxima in the Arctic, which were absent in Atlantic and Pacific profiles.

pSc from station 57 shows two large peaks, at 217 and 610 m water depths (Figure 10b), which may indicate input of detritus from the Chukchi Plateau. Indeed, these two depths mark significant changes in the slope of the Chukchi Plateau margin, supporting a margin source of detrital material to the water column. Most (~70%) of the pSc at station 57 could be explained by a detrital source, assuming upper continental crust ratios of Sc:Al. The remainder of the pSc profile at this station shows minor fluctuations. Stations 19, 48, and 52 all show peaks at ~150 m depth. The nondetrital Sc was about 50% of total pSc at the peaks at these three stations, suggesting a significant scavenged portion, and matching the high dSc observed at these depths. Small peaks of pSc in the BNL occur in the profiles of stations 48 and 52, whereas a very large peak in the BNL occurs at station 19 (Figure 10b). At station 57, collection of the lowermost sample failed, so it is not known whether an increase of pSc is associated with the BNL at that site. For comparison, data from the SE Pacific show near-bottom concentrations of pSc at stations close to the Peru margin (EPZT 1, 5) that are comparable to pSc in the Arctic (Figure 10b). Despite similar pSc concentrations between the Arctic and Pacific near-margin stations, dSc was much higher in the Arctic. Offshore stations in the EPZT transect show very low detrital and pSc concentrations (Heller et al., 2017), consistent with the low dSc (Figure 10).

4. Discussion

4.1. Uniquely High Fe/Mn Ratios in Fe-Mn Crusts and Nodules

A key difference in the Arctic crusts and nodules compared to those found elsewhere in the global ocean is the high mean Fe/Mn ratio (2.67), nearly double the previously determined highest regional mean, 1.44 for the Atlantic Ocean samples (Hein et al., 2013a). The Fe/Mn ratio determines the contents of other elements in crusts and nodules, which are acquired by sorption onto either the Fe or Mn phases depending on their seawater ionic/complex charge and the surface charge of the oxide phases (Koschinsky & Halbach, 1995; Koschinsky & Hein, 2003). Consequently, explaining this strong depletion of Mn relative to Fe is of key importance.

The Fe and Mn oxides that compose crusts precipitated from seawater and are known to have higher Fe/Mn ratios at Pacific continent-proximal sites (e.g., 1.33 for California margin seamount crusts) and in the Atlantic (Fe/Mn 1.44) and Indian Oceans (Fe/Mn 1.31) in general compared to Pacific open-ocean regions (Fe/Mn 0.74–0.96) (Hein et al., 2013a). Areas in the global ocean with higher Fe/Mn ratios have huge fluvial inputs and extensive hydrothermal systems like the Indian and Atlantic Oceans, or strong coastal upwelling, like the California margin. Likewise, the high Fe/Mn ratios for Arctic crusts can be explained by the large fluvial input, ~10% of the global discharge, to the expansive Arctic Ocean continental shelf (~53% of the Arctic Ocean area). Transport of that Fe to the basins is facilitated by brine formation on the shelves that transports shelf bottom water into the open Arctic Ocean in the halocline (Jakobsson, 2002; Timmermans et al., 2005; Van der Loeff et al., 2012). These seaward currents carry shelf-derived Fe via the "Fe shuttle," which transports Fe nanoparticles produced by redox cycling on the shelves, as described by Raiswell (2011). Dissolved Fe (dFe) is transported from the shelves to the central Arctic in the shelf-influenced halocline layer (Kondo et al., 2016). Peaks in authigenic particulate Fe (pFexs) and Mn (pMnxs) are also clearly seen at halocline depths at all four stations, supporting their shelf origin (Figure 11). The pFexs/pMnxs ratio at station 57, closest to the wide Chukchi shelf, exceeds 1.5 between 200 and 500 m, reaching a peak of 2.3 (Figure 11), approaching the mean Fe/

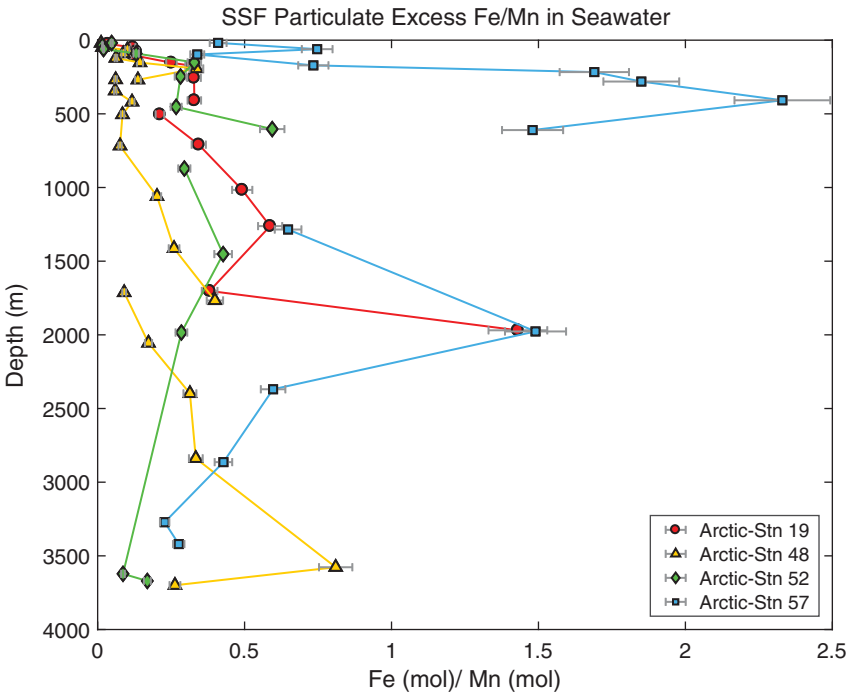

Figure 11. The ratio of authigenic particulate Fe and Mn (pFexs/pMnxs in the text), defined as the pFe and pMn in excess of lithogenic Fe and Mn; SSF = small size fraction. Error bars show RSD = 9% for pFe/pMn from repeated digestions of an internal standard.

Mn of Arctic Fe-Mn crusts, and coinciding with the depth of the general maxima in pScxs. Further away from the shelf, pFexs/pMnxs ratios decrease to less than 0.5 (Figure 10b), likely due to the much slower oxidation kinetics for Mn compared to Fe (Macdonald & Gobeil, 2012).

Shelf and upper slope bottom waters reflect the flux of elements released by redox cycling in the sediments, which has been shown to be a major source of dFe and dMn in other shelf areas (e.g., Biller & Bruland, 2013). Incorporation of Mn into the Fe-Mn crusts is controlled by the redox conditions of the water column from which it precipitates, resulting in increased dMn with lower dissolved oxygen (DO). One reason why Mn contents are so low relative to Fe, and in general in Arctic crusts, is that the OMZ in the Arctic study area is very narrow and shallow, 100–300 m in depth and coinciding with the shelf-derived halocline water mass (BCO-DMO, 2017; Kondo et al., 2016). In other areas where crusts form, the OMZ is generally broader, deeper, and more depleted in DO especially along continental margins; these characteristics are important because the OMZ provides a reservoir for the storage of high concentrations of dMn. Mn contents in the Arctic crusts are further decreased by dilution from high contents of detritus, low contents of Mn in that detritus, and the propensity for Fe oxyhydroxides to nucleate around detritus, unlike the Mn oxides, as determined by petrographic observations (see also Hein et al., 2000).

The production of dFe on shelves and upper slopes has also been related to upwelling and the width of the continental shelf (Chase et al., 2005; Vedamati et al., 2014), and particularly to the extent of a shelf mud belt, which is at 50–90 m water depths off California (Biller et al., 2013) and 50 m to the shelf edge off Peru (Bruland et al., 2005). Upwelling provides Fe required for primary productivity, which in turn provides abundant organic matter flux to the sediments that upon oxidation/degradation produces diagenetic redox zones. Suboxic conditions and seasonal hypoxia in continental shelf/slope sediments are essential to the release of dFe. For much of the global ocean, this substantial external supply of Fe is not only upwelled to promote primary productivity, but it is also advected seaward. This advected Fe and hydrothermally produced Fe are the main external sources of new dFe to the deep ocean (e.g., Fitzsimmons et al., 2017; Horner et al., 2015).

The Chukchi Sea and its broad continental shelf to the south and southwest of the study area measures 347,000 km^2 in area, with a mean water depth of only 41 m (Jakobsson, 2002). The conditions described in

the preceding paragraphs in this section are characteristic of the Chukchi shelf, where organic-matter and clay-rich areas show suboxic to anoxic conditions and have high concentrations of pFe and dFe and redox-sensitive elements (Astakhov et al., 2015; Gao et al., 2003; Kuzyk et al., 2017). Most of the sediment on the wide NW Chukchi shelf is fine grained and derived from basalt sourced from the adjacent Chukotka Peninsula and also transported through the Bering Strait (Viscosi-Shirley et al., 2003). The silt- and clay-sized sediments are distributed on the shelf by bottom currents (McManus et al., 1969), but the Si/Al ratio of the basalt (4.0) does not match the Si/Al ratios found in our Fe-Mn crusts (mean 1.75) located to the north of this wide shelf (Viscosi-Shirley et al., 2003); therefore, this basalt cannot be the dominant source of the detritus found in the crusts. However, the dFe is transported to the north off the shelf and likely contributed to the growth of the crusts. This idea is supported by a weak correlation ($r = 0.719$, $n = 9$, 97% CL) between the distance of dredge sites to the wide Chukchi shelf and mean Fe contents in the bulk crusts from each of the nine dredge hauls (dredge DS5 was excluded because it is located in a narrow rift valley that is closed and more subject to local input).

The narrow Beaufort shelf is dominated by input from the large Mackenzie River. Additional dFe and pFe input to the Arctic Ocean is derived from this and other major river systems in the Arctic region, although the largest and nearest to our study area is the Mackenzie River. Fe/Mn ratio for the Mackenzie River particulates is 95 (Gaillardet et al., 1999) and the Fe/Mn ratio for the dissolved (<0.2 μm) phases is 93 (Gaillardet et al., 2014), both of which are much higher than typical lithosphere rocks, such as MORB (Fe/Mn 57) (Gale et al., 2013), continental crust (68) (Rudnick & Gao, 2003), the Canadian Shield surface (59) (Taylor & McLennan, 1985), and PAAS shale standard (59), and many other globally important rivers (e.g., Canfield, 1997; Gaillardet et al., 1999). This fractionation of Fe and Mn during erosion and transport in the Mackenzie River system results in the input of freshwater highly enriched in Fe relative to Mn to the Beaufort shelf and transport of both dFe and pFe seaward.

Other sources of dFe and pFe are hydrothermal systems. Opening of the Canada Basin by oceanic or back-arc-basin spreading occurred during the Cretaceous and ended about 80 Myr ago (Drachev & Saunders, 2003; Lundin & Doré, 2017). Chian et al. (2016) inferred that the Canada Basin opened during a short period in the Early Cretaceous, 130–124 Myr ago. A Late Cretaceous age is indicated for the culmination of eruption of the High Arctic Large Igneous Province (HALIP), which forms part of the Mendeleev and Alpha Ridges (Drachev & Saunders, 2003; Jokat et al., 2013), and some post-Cretaceous Paleocene magmatism may also have occurred (Shimeld et al., 2016). Hydrothermal circulation associated with the seafloor production and eruption of the HALIP ceased long before Fe-Mn crusts began to form in the Amerasia Arctic Ocean ~15 Myr ago, and therefore has not been a contributing source of Fe or Mn to these crusts. The only other magmatically driven hydrothermal source of dFe and dMn in the Arctic Ocean is the ultraslow spreading Gakkel Ridge in the Eurasian Basin (Figure 1) (e.g., Edmonds et al., 2003). Venting occurs at water depths of about 2,400–3,500 m, mostly 2,900–3,500 m, and most of the hydrothermal plumes are confined to the central rift valley (Baker et al., 2004; Edmonds et al., 2003). Although Klunder et al. (2012) observed that Fe attributed to hydrothermal input from Gakkel ridge has a small influence across the Lomonosov Ridge and into the Makarov basin, it is likely that this hydrothermal source is minimal toward the Bering Strait in the Amerasia Basin relative to fluvial input and resuspension of shelf sediments.

Small-scale release of thermogenic gas on the Chukchi shelf and slope indicates that geothermal circulation may be producing metals released at the seafloor (Matveeva et al., 2015). Leaching of deep-seated rocks is common at high geothermal gradient continental margin sites (e.g., Hein et al., 2005). Although this geothermal system in the Arctic might be a source for some rare metals in the Fe-Mn crusts (e.g., Hg), it is unlikely to have provided a significant proportion of Fe and Mn to the Amerasia Arctic.

4.2. Mechanisms for Atypically Fast Growth Rates of the Arctic Fe-Mn Crusts

As mentioned, 75% of Pacific, Atlantic, and Indian Ocean crusts have average growth rates of $\leq$5 mm/Myr, with the other 25% showing rates up to about 10 mm/Myr (Hein et al., 2000). Growth rates for crusts higher than 10 mm/Myr have been considered to have a hydrothermal component, and for nodules a strong diagenetic component. However, some continental-margin crusts from those oceans, with high Fe/Mn ratios and no hydrothermal input, have growth rates of up to 20 mm/Myr (e.g., Conrad et al., 2017). The Arctic crusts show growth rates double that previous high value, up to 42 mm/Myr, with growth rates for 30 of the 92 crust samples $\geq$11 mm/Myr and 14 of those samples $\geq$20 mm/Myr. Faster than typical growth rates

for crusts without a hydrothermal component always seem to be associated with high Fe/Mn ratios; moreover, empirical evidence shows that hydrogenetic crusts with atypically fast growth rates invariably have a Fe/Mn ratio greater than one, commonly much greater than one; this is true whether growth rates were determined using isotopes or various Co chronometers (e.g., Conrad et al., 2017).

The second reason for the atypically fast growth rates is the high detrital fraction in the Arctic crusts and nodules. For open-ocean crusts, the detrital fraction is usually less than 10% and rarely up to 20% in continental-margin settings (Conrad et al., 2017; Hein et al., 2000). The detrital fraction in the Arctic crusts varies up to 35%. The high detrital component increases the accumulation rate (supporting information Table S8), provides nuclei for the growth of the oxides, especially the Fe hydroxides in some of the crust layers, and also directs the growth of the centimeters-long columns that characterize many of the Arctic crust layers (see e.g., Hein et al., 2000; Pichocki & Hoffert, 1987). Mass balance calculations indicate that the higher detrital component can increase growth rates up to ~30% over typical values, which indicates that high Fe relative to Mn is more important in explaining the up to ~300% increases over typical growth rates. Detrital mineral-mass was determined by summation of the 10 major oxides.

4.3. Host and Source for Scandium

Based on the correlation coefficients, the host for the Sc in the Fe-Mn-oxide matrix is the Fe oxyhydroxide phases. The five strongest correlations of Fe are with P, As, V, Sc, and Be. Those five elements form dissolved complexes in seawater that should sorb onto the Fe oxyhydroxides based on the electrochemical model (Koschinsky & Halbach, 1995; Koschinsky & Hein, 2003). In addition, Fe does not have positive correlations with Si indicating that Fe does not predominantly reflect silica and silicate (detrital) phases, and Sc does not correlate with Mn, indicating that it is not associated with the Mn-oxide minerals. Consequently, the high Sc contents partially reflect the high Fe-oxyhydroxide contents, on which it was sorbed. When all the data (bulk crusts, crust layers, nodules) are considered together, Sc shows weak correlations with Al and Rb, indicating that some detrital phases also host Sc, consistent with the SEM-EDX and microprobe data (see also Konstantinova et al., 2017). Thus, the anomalously high Sc contents occur because of the high Fe contents combined with the high Al-rich detrital component that is also Sc rich. The high dSc spike in the BNL for the Arctic seawater sample sites support the availability of dSc for scavenging acquisition onto Fe-oxyhydroxide phases (Figure 10a); this assumes that the BNL spike in dSc existed for much of the duration of crust growth, and it may have been historically higher based on the decrease of Sc in the crusts with time. Furthermore, this argument also applies to pSc in the Arctic seawater profiles, which shows a pSc spike in the BNL supporting its availability for incorporation into the crusts; and the scavenging of Sc by particulate phases in the water column further increases its availability for acquisition by the crusts and nodules.

Sc acquisition by the Arctic crusts and nodules decreased with time, with the older layers invariably showing higher Sc contents than the younger layers. As both the sorbed Sc and detritus-hosted Sc contributed to the total Sc content in the Arctic crusts and nodules, both sources must have changed with time; however, only the changes in the particulate source can be identified directly and the changes in paleoseawater concentrations of dSc must be inferred from the Fe oxyhydroxide-hosted Sc contents and the Fe-Mn ratios of the crusts.

4.4. Host and Source of the Atypically High Contents of As, Hg, Li, Th, and V

Relative to the average contents for the Earth's crust, As and V are enriched in typical open-ocean hydrogenetic crusts, but Hg, Li, and Th are not (Hein et al., 2003). In Arctic crusts, As and V are both among the five elements with the highest correlation coefficients with Fe, like Sc. However, unlike Sc, As and V also correlate with Mn, but to a lesser degree than with Fe, and neither correlate with Al or Si. Vanadium partitions between the Mn and Fe phases in open-ocean crusts as determined by sequential leaching, 72% with Fe and 27% with Mn, but As apparently does not, 99% with Fe (Koschinsky & Hein, 2003), so the reason for the weak correlation of As with Mn is uncertain. Based on the correlation coefficients and the Q-mode factor analyses (Figure 8 and Table 3), the additional enrichments of As and V in Arctic crusts over open-ocean crusts can be attributed to the much higher Fe relative to Mn for the Arctic crusts (supporting information Table S5). The As and V are not primarily associated with the detrital fraction.

High Hg and Li contents in crusts have been attributed to the presence of a hydrothermal component, which would then classify the deposit as having a mixed hydrogenetic-hydrothermal origin (e.g., Hein et al.,

2005). For example, high mean Hg and Li contents in Atlantic crusts compared to Pacific crusts are attributed to hydrothermal input (Hein & Koschinsky, 2014). However, a typical hydrothermal source cannot explain the Hg and Li in the Arctic crusts because hydrothermal fields did not exist in the Amerasia Arctic during the growth history of the Fe-Mn crusts.

Li can also be enriched in Mn nodules by diagenetic redox cycling in the sediment that produces Li-rich pore water that provides dLi to the nodules, however all crusts and nodules studied here are of hydrogenetic origin, not diagenetic origin, based on REY discrimination plots (Figure 5). Li is consistently high in Arctic crusts and nodules compared to hydrogenetic deposits formed elsewhere. Based on correlation coefficients and Q-mode factor analyses, the Li in the Arctic crusts and nodules is associated with many phases, but predominantly the Al-rich detritus; minor Li is associated with the residual biogenic and Fe phases. Detritus as the dominant source of Li is also supported by positive correlations with growth rate and a decrease in Li contents with time, which is also the general case for the detrital fraction. For comparison, sequential leaching of a Pacific crust and an Atlantic crust shows that about 20% of the Li is associated with the weakly leached phases (residual biogenic phases), 67% with the Mn, 13% with the detrital minerals, and none with the Fe (Koschinsky & Hein, 2003). The proportions of these components and types of detrital minerals (see below) are much different in the Arctic crusts.

Unlike Li, Hg is highly variable in the Arctic crusts and nodules and is below the detection limit (5 ppb) in many samples ($n = 33$) and up to 219 ppb ($n = 66$) with a mean of 54 ppb in the other samples. The reason for the Hg enrichments, its host phase, and its input source are difficult to pinpoint and therefore speculative. Based on Hg inorganic speciation in seawater (Byrne, 2002), it should be associated with the Fe oxyhydroxides, however, Fe is not likely the sole host for the Hg since Fe contents are consistently high in Arctic crusts but Hg contents vary from <5 ppb to 219 ppb (Table 2). Sequential leaching shows that 71% of the Hg in Pacific and Atlantic crusts is leached with the Fe phases, 13% with the Mn, 11% with the weakly leached phases, and 5% with the residual detrital minerals.

The redistribution of Hg in deep water sediments of the Amerasia Basin enriches the surface sediment relative to deeper layers in 10 cm long cores (Gobeil et al., 1999), with Hg contents of 10–116 ppb. Hg in shelf surface sediments of the northeastern Chukchi Sea correlates with the silt + clay fraction, Al, and TOC, and averages 31 ppb total Hg (range 5–55 ppb), which is considered the background concentration for that area; total dissolved Hg ranges from 0.9 to 7.0 pmol/kg (Fox et al., 2014). Based on Hg isotopes, Gleason et al. (2017) showed that Hg in Arctic Ocean sediments through time (Eocene to present) is derived from organic-carbon rich terrestrial sources and has not varied based on depositional environment, water depth, age, or climate. For the Chukchi Borderland, another possibility for Hg enrichment in some of the crusts is the geothermal hydrothermal systems that produce thermogenic gas on the Chukchi shelf (Matveeva et al., 2015). These systems leach deep-seated rocks that can supply Hg and other metals to the seafloor depending on the types of rocks leached (Hein et al., 2006), and nearby sediments on the Chukchi shelf exhibit elevated trace metals, including Hg (up to 90 ppb) (Astakhov et al., 2013). Fe-Mn crust samples from dredge site DS5, the closest site to the geothermal fracture system, had the highest mean Hg content; the mean Hg for samples from the other dredges may also reflect proximity to faults and fracture zones that are conduits for the circulation of deep-seated fluids. The non-uniform distribution of Hg does support the idea of local rather than regional sources.

Based on our statistical and compositional data, and with consideration of these cited studies of Hg in the Arctic, we suggest that Hg was sorbed onto the Fe, Mn, and biogenic phases, and is part of the detrital component of the crusts and nodules, with the source in part derived from leaching of deep-seated rocks in geothermally driven hydrothermal systems.

The mean Th content in the Arctic crusts and nodules (mean 62 ppm, max. 161 ppm) is the highest for crusts in all ocean basins, and contrasts with the mean Th of 12 ppm for central Pacific crusts. However, the Th values are only about 15% higher compared to California margin, Atlantic Ocean, and Indian Ocean crusts. In general, high Th contents in Fe-Mn crusts have been attributed to high detrital input to the depositional basin. Mean Th is also high (56 ppm) in the deep water crusts from Shatsky Rise in the NW Pacific (Hein et al., 2012b), where Th contents are strikingly high in the deepest water dredge-haul samples, 113–148 ppm Th for three bulk crusts and 152 ppm Th for a layer in one of those three crusts. Hein et al. (2012b) attributed the high Th in those crusts to the location of Shatsky Rise under the core of the Asian dust plume

and to deep water diagenetic sources of Th. dTh in the water column and Th in the Shatsky crusts both increase with increasing water depth, in contrast with Arctic crusts, which show a negative correlation of Th with water depth.

Thorium does not correlate with Si, Al, or other elements characteristic of the detrital component. The high Th in the crusts probably reflects proximity to continents with Th derived from weathering of terrestrial rocks, and the dissolution of that terrestrial material, and possibly also to the entrainment of shelf waters into the semi-isolated waters in the deep basins (Trimble et al., 2004; Van der Loeff et al., 2012). The dTh and pTh in the water column for station 3 from Trimble et al. (2004), the site closest to our study area, show near surface water and bottom water highs for ^{232}Th, the isotope characteristic of a terrigenous source. dTh can also be supplied to the basins by dissolution of biogenic silica and carbonate (Delaney & Boyle, 1983; Knauss & Ku, 1983; Moran & Moore, 1992) in the water column and sediments. Diatoms are abundant as both phytoplankton and sea ice assemblages in the Arctic Ocean.

Based on the inorganic speciation of Th in seawater (Santschi et al., 2006) and the electrochemical model for Fe-Mn crusts, Th should sorb onto the Fe oxyhydroxides. This is verified for Pacific and Atlantic crusts from sequential leaching where 99.5% of the Th leaches with the Fe oxyhydroxides (Koschinsky & Hein, 2003). For the Arctic crusts, Q-mode places Th only in the Mn-oxide factor and correlation coefficients show a strong positive correlation with Mn. However, sequential leaching is a more robust indicator, and those analyzes are in progress and are expected to be consistent with the results of Koschinsky and Hein (2003). One possible explanation is that the Fe in the Mn factor, which is commonly interpreted to reflect the Fe epitaxially intergrown with the MnO_2 (Fe-vernadite), reflects a combination of Mn phases and amorphous Fe phases. This could account for the Th in the Mn factor. In this case, Factor 3, the Fe factor, would reflect goethite and other crystalline Fe phases. However, the low rotated factor score (0.14) of Fe in the Mn factor does not fully support this idea.

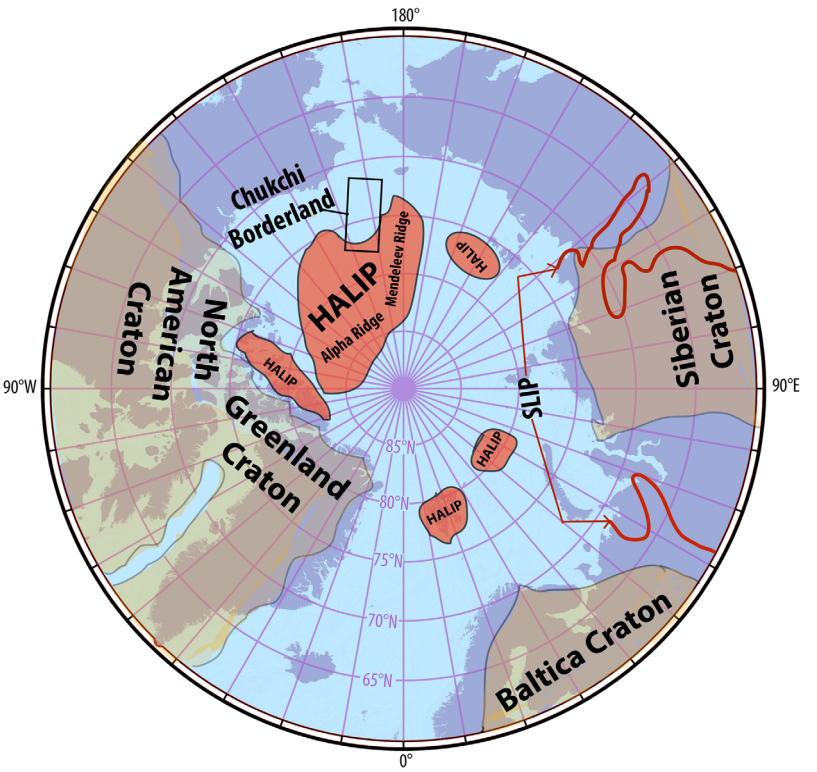

Figure 12. Map showing generalized distributions of cratons and the High Arctic and Siberian Large Igneous Provinces (HALIP, SLIP) in and around the Arctic Ocean; black box encloses much of the Chukchi Borderland. HALIP data from Døssing et al. (2013); also see Oakey and Saltus (2016) for a detailed distribution; cratons from Pease et al. (2014); and SLIP from Czamanske and Fedorenko (2004).

4.5. Source of the High and Unique Detrital Component of the Fe-Mn Crusts

The Arctic Ocean is unique among ocean basins in that it is surrounded predominantly by cratons, as well as two large igneous provinces (LIP), the HALIP of mostly Cretaceous age (e.g., Bruvoll et al., 2012; Døssing et al., 2013) and the Siberian LIP (SLIP) of mostly Late Permian and Early Triassic ages (e.g., Kamo et al., 2003; Wooden et al., 1993) (Figure 12). In addition, Paleozoic continental blocks occur within the Arctic Ocean, for example the Chukchi Borderland and Northwind Ridge (e.g., Brumley et al., 2015; Grantz et al., 1998; O'Brien et al., 2016). The Mendeleev and Alpha Ridges are composed predominantly of HALIP rocks (e.g., Bruvoll et al., 2012; Oakey & Saltus, 2016) and partly of continental rocks (Gusev et al., 2017; Morozov et al., 2013; Vernikovsky et al., 2014). The Fe-Mn crusts in the Amerasia Arctic grew on rocks of the HALIP and also continental rocks, and acquired detritus from weathering of those substrates.

As mentioned above, the detrital component of the Arctic Fe-Mn crusts and nodules is much larger than for crusts collected elsewhere in the global ocean, and in addition, the composition of the detritus is much different than for other crusts. The detrital fraction of Pacific Fe-Mn crusts consists typically of quartz, feldspar, magnetite, titanomagnetite, clay minerals, and depending on location, other minor trace minerals. In contrast, the Arctic crusts contain a wide variety of detrital minerals, that in addition to quartz and feldspars, include pyroxene, amphibole, magnetite, dolomite, and clay minerals identified by XRD, and zircon, apatite, monazite, xenotime, rutile, ilmenite, titanite, franklinite, gypsum, and barite identified using SEM-EDX and microprobe (examples in Figure 6). Additionally, some detrital metal oxides, carbonates, and silicates have been identified that may indicate input from erosion of ancient mineral deposits, such as Cu-, Zn-, Pb-, Ni-, Zr-, and Cr-rich minerals—these kinds of ore minerals have not previously been found in open-ocean hydrogenetic Fe-Mn crusts, with the exception of Cr-spinel (e.g., Hein et al., 2000). Many of these minerals indicate mafic and especially ultramafic source rocks, such as gabbro, peridotite, pyroxenite, carbonatite, and metamorphic amphibolite, and other rocks characteristic of continental igneous and metamorphic sources. In the Amerasia Arctic, amphibolite, gneiss, and granite were dredged from the Chukchi Borderland (Brumley et al., 2015). Moreover, ultramafic rocks likely comprise a large part of the HALIP that makes up much of the Mendeleev and Alpha Ridges (Oakey & Saltus, 2016).

The mechanisms of transport of these detrital minerals to the depositional basin include continental erosion and input via rivers and at times glaciers, and distribution by sea ice, brine plumes and current systems. Wind-blown dust is considered a minor source of detritus. Erosion of outcrops on the Chukchi Borderland, Mendeleev Ridge, and Alpha Ridge are also likely common sources for the detrital minerals, but have not been considered in past studies (Dausmann et al., 2015) primarily because isotopic data do not exist for those rocks. The formation of sea ice in the Amerasia Arctic would host sediment transported from the surrounding area, especially from the East Siberian and Laptev Sea shelves.

As mentioned above, the Si/Al ratios of the Arctic Fe-Mn crusts are also atypical of Fe-Mn crusts from other areas, for example mean Si/Al is 2.37, 3.73, 4.00, and 6.18 for Atlantic, Indian, central Pacific, and California margin crusts, respectively (Conrad et al., 2017; Hein et al., 2013a, 2013b). The low ratios for the Arctic crusts (mean 1.75) and nodules (mean 1.64) are most comparable to Alpha Ridge altered rocks (1.86) (Van Wagoner et al., 1986), Mackenzie River clay-sized particulates, mean 2.10 (Bayon et al., 2015), Mendeleev Ridge basalt and andesite, and Chukchi Borderland basalt, means 2.31, 2.48, and 2.49 respectively (Morozov et al., 2013; Mukasa et al., 2009). Other potential sources of rocks with some relatively low Si/Al ratios are amphibolite and pyroxenite; although data are not available for rocks from the Arctic Ocean, data from other geological sections show a wide range of ratios. For example in Korea, amphibolite Si/Al ranges from 1.03 to 3.14, mean 1.94 (So, 1978) and for Sierra Nevada, California, low-MgO pyroxenite Si/Al ranges from 2.18 to 3.85, mean 2.40 (Lee et al., 2006); another possible source is lower continental crust (2.79) (Rudnick & Gao, 2003). Si/Al for SLIP basalt also varies widely, with means from six different geological sections ranging from 2.79 to 3.03 (Sharma et al., 1991; Wooden et al., 1993), and Russian shale composite with a Si/Al ratio of 2.84 (Viscosi-Shirley et al., 2003). Additional potential source areas are undifferentiated Mackenzie River particulates, Si/Al 3.45 (Gaillardet et al., 1999) and 3.78 (Martin & Meybeck, 1979), and upper continental crust, Si/Al 3.82 (Rudnick & Gao, 2003), although these have higher mean Si/Al ratios than found in the Arctic Fe-Mn crusts.

Alternatively, or in addition, the high Al relative to Si might be due in part to preferential sorption of Al by Fe oxyhydroxide minerals which when combined with the Al in the detrital minerals would increase the

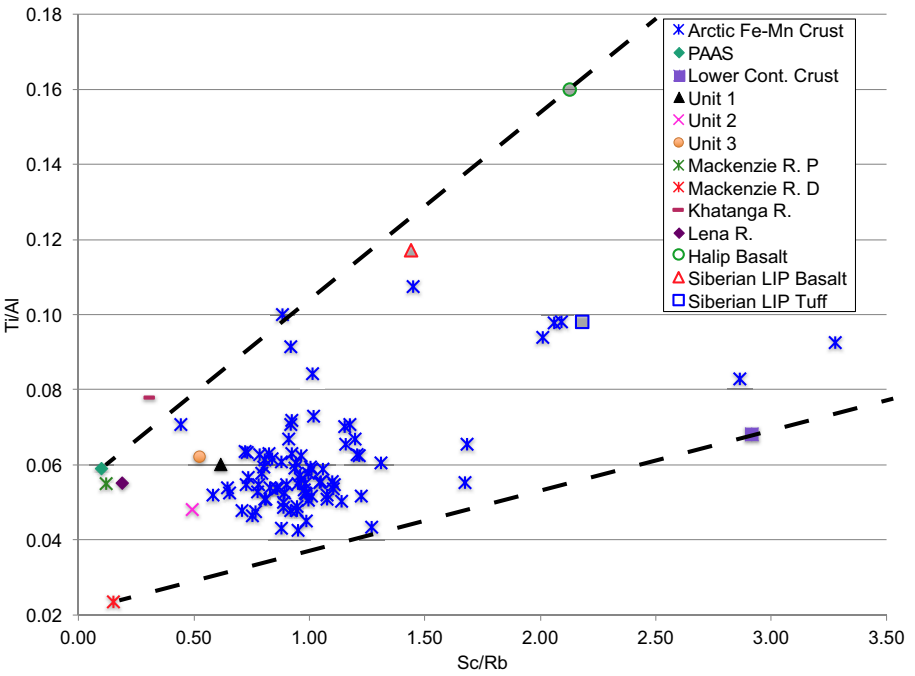

Figure 13. Geochemical source area discrimination plot after Martinez et al. (2009). Four end-members can explain our entire data set: average shale (PAAS), the High Arctic Large Igneous Province (HALIP Mendeleev Ridge basalt) (Morozov et al., 2013), the Mackenzie River (Gaillardet et al., 1999, 2014), and lower continental crust. Dissolved Sc data were not found for the Mackenzie River or other Canada rivers; the Ti/Al ratio for the Mackenzie River dissolved phase is 0.0235 but the Sc/Rb ratio is not known, so the ratio for the particulate phase is used, which ranges from 0.078 to 0.206 (Gaillardet et al., 1999; Vonk et al., 2015). D and P after River (R.) in the key mean dissolved and particulate phases respectively; units 1–3 are for a IODP 302 composite 428 m core from Lomonosov Ridge; unit 1 is late Eocene through Holocene, unit 2 is middle Eocene, and unit 3 is Late Cretaceous through early Eocene (Martinez et al., 2009). Siberian LIP basalt from Wooden et al. (1993) and Siberian LIP tuff from Büchl and Gier (2003).

total Al relative to total Si content of the Fe-Mn crusts. Sequential leaching of Pacific Fe-Mn crusts (non-phosphatized) shows sorption of Al and Si by both the Mn oxide and Fe oxyhydroxide minerals, 18% of Si with Mn and 28% with Fe, and 13% of Al with Mn and 38% with Fe (Koschinsky & Halbach, 1995). With the high Fe versus Mn contents of Arctic Fe-Mn crusts and the preferential sorption of Al on Fe oxyhydroxides, the ~10% differential of Al sorption by Fe compared to Si might explain some part of the low Si/Al ratios.

Another approach to determining possible sources of the detrital component is to use a discrimination plot to compare our data with potential source areas, and we chose the Ti/Al versus Sc/Rb diagram, after Martinez et al. (2009). All of our geochemical data are enclosed within an area defined by four potential end-members: Average shale (PAAS; typical average upper continental crust) and HALIP (Mendeleev Ridge basalt) (Morozov et al., 2013); the Mackenzie River (Gaillardet et al., 1999, 2014) and lower continental crust (Figure 13). Dissolved Sc data apparently do not exist for the Mackenzie River or any other Canada rivers (Gaillardet et al., 2014); the Ti/Al ratio for the Mackenzie River dissolved phase is 0.0235 but the Sc/Rb ratio is not known, so the ratio for the particulate phase is used, which ranges from 0.078 to 0.206 (Gaillardet et al., 1999; Vonk et al., 2015). In addition, the SLIP rocks could also have been a source for detrital minerals in many of our Fe-Mn crusts.

Sediments from Lomonosov Ridge in the central Arctic Ocean that are the same age as our Fe-Mn crusts, were suggested to have been formed predominantly from a source with a composition like shale (units 1 and 3, Figure 13), such as weathering of surficial continental crust from northern Russia (Martinez et al., 2009). Likewise, most of our samples plot near the shale/Mackenzie River apex on our discrimination plot (Figure 13). However, that cannot be the only source of detritus in our samples and various contributions from the other end-members in Figure 13 must be considered, including potential sources indicated by the Si/Al ratios for which we do not have data, such as the Mackenzie River clay-sized material for which the Ti/Al is 0.041 (Bayon et al., 2015), but the Rb and Sc values are not known. The most likely sources in addition

to the contributions from North America via rivers and glaciers are local deep water outcrops, such as the HALIP, including the mafic and ultramafic components that comprise much of the Mendeleev and Alpha Ridges, as well as continental and lower crustal rocks from the Chukchi Plateau.

4.6. Temporal Changes in Composition

The initiation of growth of most Fe-Mn crusts studied here was post 10 Myr ago, with the oldest five crusts (6% of the total) varying between 14.8 and 10.2 Myr; 44% started growing between 10 and 6 Myr ago, and 50% between 6 and 0.7 Myr ago. Many of the younger crusts may have started growing on more recently exposed rock surfaces, or older crusts destroyed by gravity processes such as mass movements, which is common for crusts formed elsewhere in the global ocean (e.g., Hein et al., 2000).

Given that the Arctic Ocean existed in the Cretaceous, albeit as a freshwater lake into the early Cenozoic (Hegewald & Jokat, 2013; Moran et al., 2006), why did it take so long for Fe-Mn crusts to form in the Amerasia Arctic Ocean? The main reasons focus on the establishment of modern-type circulation through opening of the Fram Strait to deep water exchange with the North Atlantic Ocean, a shift from variable ventilation to a fully ventilated Arctic Ocean, and little ice rafting in the central Arctic during the Miocene climate optimum; all of these changes occurred circa 17.5–16 Myr ago (e.g., Jakobsson et al., 2007; St. John, 2008). These were key steps in preparing the Amerasia Arctic Ocean for conditions necessary for the precipitation of Fe-Mn crusts from seawater. Middle Miocene cooling, the change from seasonal to perennial sea ice, continued deepening of the Fram Strait and ventilation of the Amerasia Arctic, and enhanced brine formation (e.g., Haley et al., 2008; Martinez et al., 2009; Moran et al., 2006) completed the conditions necessary for the widespread growth of Fe-Mn crusts. The tectonic and geological stability of the Amerasia Arctic was also important for preservation of the crusts. For example, from ~22 to 14 Myr ago the Amerasia Arctic experienced late-stage tectonic extension of Mendeleev and Alpha Ridges accompanied by local igneous intrusions (Bruvoll et al., 2012). Of all these contributing factors, the crusts could not have formed without ventilation of the deep waters. Three of the five oldest crusts (14.8, 10.8, and 10.3 Myr old) come from dredge haul DR5, which is the deepest water site, 3,851 m (Table 1). These data indicate that by circa 15 Myr ago, the Amerasia Arctic Ocean basins were ventilated to depths below the Arctic Intermediate Water.

Temporal changes in crust chemistry and mineralogy were mentioned in previous sections, where Mn and associated elements increased and detrital-associated elements decreased with time (supporting information Table S5); both the detritus-associated elements and Fe oxyhydroxide-associated Sc generally decreased with time. These changes have facilitated the development of Fe-Mn crusts more like those found in the rest of the global ocean, although not entirely so. Paleoceanographic conditions fluctuated throughout the Neogene, but conditions that likely contributed to the temporal geochemical trends in crusts include the extent of sea ice, which varied from perennial in the Miocene to nearly sea ice free for much of the Pliocene (~5.3 to ~2.6 Myr ago) (e.g., Brigham-Grette et al., 2013; Cronin et al., 1993; Frank et al., 2008; Matthiessen et al., 2009; Scott et al., 1989), followed by Pleistocene cooling, and then a return to perennial sea ice. The extent of sea ice determined the relative amounts of sedimentation from sea ice versus from icebergs sourced from the continental margins. Glaciation determined the amount of mechanical versus chemical weathering on the cratons that delivered variable types and sizes of sediment to the Arctic Ocean via icebergs and rivers (e.g., Dausmann et al., 2015; Moran et al., 2006; Scott et al., 1989).

While these regional and Arctic Ocean-wide temporal changes influenced the composition and growth of crusts (Dausmann et al., 2015), the history of each crust is complicated by local conditions, such as by the differences in the local geological and oceanographic settings. These local environmental characteristics explain why the timing of distinct textural changes in the crusts varies among the set of crusts studied. Three or four distinct layers characterize most of the older, thicker crusts, however, local conditions controlled the variations in thickness, texture, and boundary ages of the layers for this group of Amerasia Arctic Ocean crusts.

5. Conclusions and Summary

Ferromanganese crusts and nodules collected during 2008, 2009, and 2012 cruises to the Amerasia Arctic Ocean are characterized by unique mineral and chemical compositions, fast growth rates, and other characteristics compared to crusts formed elsewhere in the global ocean. These characteristics reflect temporal

and spatial variations in geological, oceanographic, and climatic conditions in the Arctic Ocean and surrounding continents over the past ~15 Myr.

Initiation of Arctic Fe-Mn crust growth was ~15 Myr ago. The start of crust growth in the Amerasia Arctic is attributed to establishment of modern-type circulation starting with the deepening of Fram Strait in the North Atlantic Ocean, which occurred ~17.5 to 16.0 Myr ago. The most significant event for initiation of crust growth was ventilation of the deep basins of the Amerasia Arctic, which accompanied with middle Miocene cooling and tectonic stability, established the conditions necessary for the widespread growth of the Fe-Mn crusts. These data indicate that by circa 15 Myr ago, the Amerasia Arctic Ocean basins were ventilated to depths below the Arctic Intermediate Water. Neogene environmental changes determined the sources and mechanisms of transportation of dissolved and particulate phases that affected the composition and growth of crusts. While these regional and Arctic Ocean-wide temporal changes influenced the composition and growth of crusts, the history of each crust was complicated by local geological and oceanographic conditions.

The exceptionally fast growth rates for Arctic Fe-Mn crusts vary from 1.1 to 42.1 mm/Myr for all samples. High growth rates (>10 mm/Myr) are usually considered to reflect hydrothermal input. However, the high Fe contents relative to Mn, and the large detrital component combined to significantly increase growth rates compared to crusts formed elsewhere in the global ocean. Therefore, thick Arctic Ocean hydrogenetic crusts can form over much shorter time periods than those found elsewhere in the global ocean. Based on data presented here and Conrad et al. (2017), the range of growth rates for hydrogenetic crusts seems to be increasing as new environments are being studied.

The high detrital mineral content consists predominantly of quartz, feldspar, pyroxene, amphibole, magnetite, dolomite, and clay minerals along with many trace minerals, such as detrital high Cu-, Zn-, Pb-, Ni-, Zr-, Cr-minerals; these metal-rich minerals may have been derived from weathering of ancient mineral deposits. Many of the detrital minerals are typical of mafic and especially ultramafic rocks, like those recovered from the Chukchi Platform, and Mendeleev and Alpha Ridges. Erosion of local outcrops from these three areas is likely the main source of detritus for the crusts, along with contributions from North America and Siberia, which are transported via rivers and glaciers and dispersed via sea ice, brine plumes, and current systems.

Discrimination diagrams show that the crusts and nodules are hydrogenetic. However, the oxide mineralogy is atypical for hydrogenetic Fe-Mn crusts and nodules, which typically include only amorphous Fe oxyhydroxide and δ-MnO_2 (vernadite). In contrast, the Arctic samples also include the Mn oxides birnessite, 10 Å manganates (predominantly todorokite), and rarely ramsdellite, and the Fe minerals also include goethite, lepidocrocite, feroxyhyte, and ferrihydrite. These differences reflect formation under lower oxygen conditions for the Arctic crusts compared to those found elsewhere, and are most similar to crusts formed in continental-margin environments.

The unique difference in chemical composition between Arctic crusts and those formed elsewhere is the high Fe contents relative to Mn, which determines the trace elements hosted by Fe-Mn oxide phases and their concentrations. The high Fe/Mn ratios reflect the expansive continental shelves and upper slopes that support redox cycling that releases Fe to bottom waters, and to the large fluvial input from North America and Siberia. Brine formation on the shelves promotes the distribution of the Fe throughout the Amerasia Arctic Ocean including the deep basins. The very low Mn contents in Arctic crusts reflect the OMZ in the Arctic study area, which is very narrow and shallow, 100–300 m (BCO-DMO, 2017; Kondo et al., 2016). In other areas where crusts form, the OMZ is broader, deeper, and more depleted in DO, especially along continental margins. This is important because the OMZ provides a reservoir for the storage of high concentrations of dMn. Mn contents in Arctic crusts are further decreased by dilution from high detritus contents, low contents of Mn in that detritus, and the propensity for Fe oxyhydroxides to nucleate around detritus.

Uniquely high contents of Sc in Arctic crusts and nodules set them apart from Fe-Mn deposits formed elsewhere in the global ocean. The Sc content decreased in the crusts with time. Sc was sorbed on the Fe oxyhydroxide matrix and is also part of the Al-rich component of the detrital fraction. dSc and pSc seawater profiles in Amerasia Arctic Ocean show the highest concentrations at the sites closest to Mackenzie River and continental shelf and Sc maxima are related to the halocline and other shelf processes including production of brine plumes. Spikes in dSc and pSc concentrations within the BNL attest to their availability for sorption onto the Fe phases and acquisition as detrital minerals.

Arctic Ocean crusts and nodules also have high contents of As, V, Li, Hg, and Th compared to crusts from the other oceans. The high As, V, and Th contents reflect the higher Fe relative to Mn contents for Arctic crusts and nodules. As, V, and Th sorb predominantly onto the Fe oxyhydroxide minerals. Li is likely a component of many crust and nodule phases, but the most significant associations are with the Al-rich detrital phases, with a small component of the Li associated with the residual biogenic and Fe phases. The key difference of Hg in the crusts is its high content and variability compared to the other elements with unusually high contents. Hg in the Arctic Fe-Mn deposits is hosted by the Fe and Mn matrix phases in addition to the detrital and biogenic phases. The source of the Hg is likely nearby geothermal hydrothermal systems that release Hg and other trace metals to the seafloor, and also detrital organic-carbon rich terrestrial sediments.

Based on temporal changes recorded in the crusts, the elements occur in three groups: (1) progressively higher concentrations with time (Mn, Ni, Co, Ca, Bi, Pb, Se, Te, Th, Tl, La, Pr, Nd, Sm); (2) progressively lower concentrations with time (Al, K, Cs, Ga, Li, and Sc); (3) and variable with time. The changes indicate that the Arctic crusts are becoming more like crusts from elsewhere in the global ocean as the Fe/Mn ratio and detritus decrease.

Acknowledgments

We thank Kelley J. Brumley for sample collection and curation at sea and Brian Buczkowski for sample curation onshore; Elizabeth Miller, Kate Maher, and Ginger Barth provided useful discussions. We thank Simone Moos, Gabi Weiss, the pumping group (Maija Heller, Erin Black, Lauren Kipp, and Steven Pike), Greg Cutter, Dave Kadko, and Bill Landing for GEOTRACES sample collection at sea, as well as Luz Romero for help with ICP-MS analyses at Texas A&M and Rob Franks from the Marine Analytical Lab for ICP-MS for help at UCSC. We thank Larry A. Mayer, chief scientist, and the Captain and crew of the USCGC icebreaker *Healy* cruises HLY0805, HLY0905, and HLY1202. We thank Leslie Hayden for help with the microprobe and SEM-EDX data collection and reduction and Tracey Conrad and Francesca Spinardi for considerable help with lab work. We also thank the U.S. Extended Continental Shelf program for providing the samples used in this study, especially the Department of State as lead agency (Brain van Pay), the U.S. Geological Survey (Deborah Hutchinson and Brian Buczkowski), and NOAA (Carla Moore). Thomas Kuhn, BGR, Hanover Germany, and an anonymous reviewer provided helpful comments that improved this paper; Carol Reiss provided a valuable internal USGS review. J.N.F was funded by the National Science Foundation (OCE 1434493 and 1713677). P.J.L., Y.X., and K.M. were partially supported by NSF-OCE 1535854. The IGSN numbers of the samples used here are in supporting information Table S9. The data used in this paper can be found in the figures and tables in the paper and supporting information.

References

Amakawa, H., Nomura, M., Sasaki, K., Oura, Y., & Ebihara, M. (2007). Vertical distribution of scandium in the north central Pacific. *Geophysical Research Letters*, *34*, L11606. https://doi.org/10.1029/2007GL029903

Anders, E., & Grevesse, N. (1989). Abundances of the elements: Meteoritic and solar. *Geochimica et Cosmochimica Acta*, *53*, 197–214. https://doi.org/10.1016/0016-7037(89)90286-X

Astakhov, A. S., Bosin, A. A., Kolesnik, A. N., & Obrezkova, M. S. (2015). Sediment geochemistry and diatom distribution in the Chukchi Sea. *Oceanography*, *28*, 190–201. https://doi.org/10.5670/oceanog.2015.65

Astakhov, A. S., Gusev, E. A., Kolesnik, A. N., & Shakirov, R. B. (2013). Conditions of the accumulation of organic matter and metals in the bottom sediments of the Chukchi Sea. *Russian Geology and Geophysics*, *54*, 1056–1070. https://doi.org/10.1016/j.rgg.2013.07.019

Baker, E. T., Edmonds, H. N., Michael, P. J., Bach, W., Dick, H. J. B., Snow, J. E., . . . Langmuir, C. H. (2004). Hydrothermal venting in magma deserts: The ultraslow-spreading Gakkel and Southwest Indian Ridges. *Geochemistry, Geophysics, Geosystems*, *5*, Q08002. https://doi.org/10.1029/2004GC000712

Bau, M., Schmidt, K., Koschinsky, A., Hein, J., Kuhn, T., & Usui, A. (2014). Discriminating between different genetic types of marine ferro-manganese crusts and nodules based on rare earth elements and yttrium. *Chemical Geology*, *381*, 1–9. https://doi.org/10.1016/j.chemgeo.2014.05.004

Bayon, G., Toucanne, S., Skonieczny, C., André, L., Bermell, S., Cheron, S., . . . Barrat, J. A. (2015). Rare earth elements and neodymium isotopes in world river sediments revisited. *Geochimica et Cosmochimica Acta*, *170*, 17–38. https://doi.org/10.1016/j.gca.2015.08.001

BCO-DMO. (2017). *Introduction to BCO-DMO*. Washington. DC: Author. Retrieved from http://www.bco-dmo.org/dataset/647259

Biller, D. V., & Bruland, K. W. (2012). Analysis of Mn, Fe, Co, Ni, Cu, Zn, Cd, and Pb in seawater using the Nobias-chelate PA1 resin and magnetic sector inductively coupled plasma mass spectrometry [ICP-MS]. *Marine Chemistry*, *130–131*, 12–20. https://doi.org/10.1016/j.marchem.2011.12.001

Biller, D. V., & Bruland, K. W. (2013). Source and distributions of Mn, Fe, Co, Ni, Cu, Zn, and Cd relative to macronutrients along the central California coast during the spring and summer upwelling season. *Marine Chemistry*, *155*, 50–70. https://doi.org/10.1016/j.marchem.2013.06.003

Biller, D. V., Coale, T. H., Till, R. C., Smith, G. J., & Bruland, K. W. (2013). Coastal iron and nitrate distributions during the spring and summer upwelling season in the central California Current upwelling regime. *Continental Shelf Research*, *66*, 58–72. https://doi.org/10.1016/j.csr.2013.07.003

Björk, G., Jakobsson, M., Rudels, B., Swift, J. H., Anderson, L., Darby, D. A., . . . Edwards, M. (2007). Bathymetry and deep-water exchange across the central Lomonosov Ridge at 88–89° N. *Deep-Sea Research Part I: Oceanographic Research Papers*, *54*, 1197–1208. https://doi.org/10.1016/j.dsr.2007.05.010

Brigham-Grette, J., Melles, M., Minyuk, P., Andreev, A., Tarasov, P., DeConto, R., . . . Herzschuh, U. (2013). Pliocene warmth, polar amplification, and stepped Pleistocene cooling recorded in NE Arctic Russia. *Science*, *340*, 1421–1427. https://doi.org/10.1126/science.1233137

Bruland, K. W., Rue, E. L., Smith, G. J., & DiTullio, G. R. (2005). Iron, macronutrients and diatom blooms in the Peru upwelling regime: brown and blue waters of Peru. *Marine Chemistry*, *93*, 81–103.

Brumley, K., Miller, E. L., Konstantinou, A., Grove, M., Meisling, K. E., & Mayer, L. A. (2015). First bedrock samples dredged from submarine outcrops in the Chukchi Borderland, Arctic Ocean. *Geosphere*, *11*, 76–92. https://doi.org/10.1130/GES01044.1

Bruvoll, V., Kristoffersen, Y., Coakley, B. J., Hopper, J. R., Planke, S., & Kandilarov, A. (2012). The nature of the acoustic basement on Mendeleev and northwestern Alpha ridges, Arctic Ocean. *Tectonophysics*, *514–517*, 123–145. https://doi.org/10.1016/j.tecto.2011.10.015

Büchl, A., & Gier, S. (2003). Petrogenesis and alteration of tuffs associated with continental flood basalts from Putorana, northern Siberia. *Geological Magazine*, *140*, 649–659. https://doi.org/10.1017/S0016756803008392

Byrne, R. H. (2002). Inorganic speciation of dissolved elements in seawater: The influence of pH on concentration ratios. *Geochemical Transactions*, *3*(2), 11–16. https://doi.org/10.1186/1467-4866-3-11

Canfield, D. E. (1997). Geochemistry of river particulates from the continental USA: Major elements. *Geochimica et Cosmochimica Acta*, *61*, 3349–3365. https://doi.org/10.1016/S0016-7037(97)00172-5

Chase, Z., Johnson, K. S., Elrod, V. A., Plant, J. N., Fitzwater, S. E., Pickell, L., & Sakamoto, C. M. (2005). Manganese and iron distributions off central California influenced by upwelling and shelf width. *Marine Chemistry*, *95*, 235–254. https://doi.org/10.1016/j.marchem.2004.09.006

Chian, D., Jackson, H. R., Hutchinson, D. R., Shimeld, J. W., Oakey, G. N., Lebedeva-Ivanova, N., . . . Mosher, D. C. (2016). Distribution of crustal types in Canada Basin, Arctic Ocean. *Tectonophysics*, *691*, 8–30.

Clark, D. L., Whitman, R. R., Morgan, K. A., & Mackey, S. D. (1980). Stratigraphy and glacial-marine sediment of the Amerasia Basin, central Arctic Ocean, *Geological Society of America Special Paper*, *181*, 57. https://doi.org/10.1130/SPE181-p1

Conrad, T., Hein, J. R., Paytan, A., & Clague, D. A. (2017). Formation of Fe-Mn crusts within a continental margin environment. *Ore Geology Reviews*, *87*, 25–40. https://doi.org/10.1016/j.oregeorev.2016.09.010

Cook, H. E., Johnson, P. D., Matti, J. C., & Zemmels, I. (1975). Methods of sample preparation and X-ray diffraction data analysis, X-ray mineralogy laboratory, Deep Sea Drilling Project, University of California Riverside. In *Initial reports of the deep sea drilling project* (Vol. 28, pp. 999–1001). Washington, DC: U.S. Government Printing Office. https://doi.org/10.2973/dsdp.proc.28.app4.1975

Cronin, T. M., Whatley, R., Wood, A., Tsukagoshi, A., Ikeya, H., Brouwers, E. M., & Briggs, W. M. Jr. (1993). Microfaunal evidence for elevated Pliocene temperatures in the Arctic Ocean. *Paleoceanography*, *8*, 161–173. https://doi.org/10.1029/93PA00060

Cullen, J. T., & Sherrell, R. M. (1999). Techniques for determination of trace metals in small samples of size-fractionated particulate matter: Phytoplankton metals off central California. *Marine Chemistry*, *67*, 233–247. https://doi.org/10.1016/S0304-4203(99)00060-2

Cutter, G. A., & Bruland, K. W. (2012). Rapid and noncontaminating sampling system for trace elements in a global ocean surveys. *Limnology & Oceanography: Methods*, *10*, 425–436. https://doi.org/10.4319/lom.2012.10.425

Czamanske, G. K., & Fedorenko, V. A. (2004). The demise of the Siberian plume. Mantleplumes. Retrieved from http://www.mantleplumes.org/WebpagePDFs/Siberia.pdf

Dausmann, V., Frank, M., Siebert, C., Christl, M., & Hein, J. R. (2015). The evolution of climatically driven weathering inputs into the western Arctic Ocean since the late Miocene: Radiogenic isotope evidence. *Earth and Planetary Science Letters*, *419*, 111–124. https://doi.org/10.1016/j.epsl.2015.03.007

Delaney, M. L., & Boyle, E. A. (1983). Uranium and thorium isotope concentrations in foraminiferal calcite. *Earth and Planetary Science Letters*, *62*, 258–262. https://doi.org/10.1016/0012-821X(83)90088-2

Døssing, A., Jackson, H. R., Matzka, J., Einarsson, I., Rasmussen, T. M., Olesen, A. V., & Brozena, J. M. (2013). On the origin of the Amerasia Basin and the High Arctic Large Igneous Province—Results of new aeromagnetic data. *Earth and Planetary Science Letters*, *363*, 219–230. https://doi.org/10.1016/j.epsl.2012.12.013

Drachev, S., & Saunders, A. (2003). The early Cretaceous Arctic LIP: Its geodynamic setting and implications of Canada Basin opening. In R. Scott and D. Thurston (Eds.), *Proceedings of fourth international conference on Arctic margins* (pp. 206–215). Anchorage, AK: U.S. Department of the Interior Minerals Management Service.

Edmonds, H. N., Michael, P. J., Baker, E. T., Connelly, D. P., Snow, J. E., Langmuir, C. H., . . . Graham, D. W. (2003). Discovery of abundant hydrothermal venting on the ultraslow-spreading Gakkel ridge in the Arctic Ocean. *Nature*, *421*, 252–256. https://doi.org/10.1038/nature01351

Engleman, E. E., Jackson, L. L., Norton, D. R., & Fischer, A. G. (1985). Determinations of carbonate carbon in geological materials by coulometric titration. *Chemical Geology*, *53*, 125–128. https://doi.org/10.1016/0009-2541(85)90025-7

Fitzsimmons, J. N., John, S. G., Marsay, C. M., Hoffman, C. L., Nicholas, S. L., Toner, B. M., . . . Sherrell, R. M. (2017). Iron persistence in a distal hydrothermal plume supported by dissolved-particulate exchange. *Nature Geoscience*, *10*, 195–201. https://doi.org/10.1038/NGEO2900

Fox, A. L., Hughes, E. A., Trocine, R. P., Trefry, J. H., Schonberg, S. V., McTigue, N. D., . . . Cooper, L. W. (2014). Mercury in the northeastern Chukchi Sea: Distribution patterns in seawater and sediments and biomagnification in the benthic food web. *Deep-Sea Research Part II: Topical Studies in Oceanography*, *102*, 56–67. https://doi.org/10.1016/j.dsr2.2013.07.012

Frank, M., Backman, J., Jakobsson, M., Moran, K., O'regan, M., King, J., . . . Garbe-Schönberg, D. (2008). Beryllium isotopes in central Arctic Ocean sediments over the past 12.3 million years: Stratigraphic and paleoclimatic implications. *Paleoceanography*, *23*, PA1S02. https://doi.org/10.1029/2007PA001478

Frank, M., O'nions, R. K., Hein, J. R., & Banakar, V. K. (1999). 60 Myr records of major elements and Pb-Nd isotopes from hydrogenous ferromanganese crusts: Reconstruction of seawater paleochemistry. *Geochimica et Cosmochimica Acta*, *63*, 1689–1708. https://doi.org/10.1016/S0016-7037(99)00079-4

Gaillardet, J., Dupré, B., & Allègre, C. J. (1999). Geochemistry of large river suspended sediments: Silicate weathering or recycling tracer? *Geochimica Et Cosmochimica Acta*, *63*, 4037–4051. https://doi.org/10.1016/S0016-7037(99)00307-5

Gaillardet, J., Viers, J., & Dupré, B. (2014). Trace elements in river waters. In H. D. Holland and K. K. Turekian (Eds.), *Treatise on geochemistry* (2nd ed., Vol. 7, Chapter 7, pp. 195–235). Oxford, UK: Elsevier. https://doi.org/10.1016/B978-0-08-095975-7.00507-6

Gale, A., Dalton, C. A., Langmuir, C. H., Su, Y., & Schilling, J. G. (2013). The mean composition of ocean ridge basalts. *Geochemistry, Geophysics, Geosystems*, *14*, 489–518. https://doi.org/10.1029/2012GC004334

Gao, A., Liu, Y., Zhang, D., & Sun, H. (2003). Latitudinal distribution of iodine in sediments in the Chukchi Sea and the Bering Sea. *Science in China, Series D*, *46*, 592–602. https://doi.org/10.1007/BF02984537

Gladenkov, A. Y., Oleinik, A. E., Marincovich, L. Jr., & Barinov, K. B. (2002). A refined age for the earliest opening of Bering Strait. *Palaeogeography, Palaeoclimatology, Palaeoecology*, *183*, 321–328. https://doi.org/10.1016/S0031-0182(02)00249-3

Gleason, J. D., Blum, J. D., Moore, T. C., Polyak, L., Jakobsson, M., Meyers, P. A., & Biswas, A. (2017). Sources and cycling of mercury in the paleo Arctic Ocean from Hg stable isotope variations in Eocene and Quaternary sediments. *Geochimica et Cosmochimica Acta*, *197*, 245–262. https://doi.org/10.1016/j.gca.2016.10.033

Gobeil, C., MacDonald, R. W., & Smith, J. N. (1999). Mercury profiles in sediments of the Arctic Ocean basins. *Environmental Science and Technology*, *33*, 4194–4198. https://doi.org/10.1021/es990471p

Grantz, A., Clark, D. L., Phillips, R. L., & Srivastava, S. P. (1998). Phanerozoic stratigraphy of Northwind Ridge, magnetic anomalies in the Canada basin, and the geometry and timing of rifting in the Amerasia basin, Arctic Ocean. *Geological Society of America Bulletin*, *110*, 801–820. https://doi.org/10.1130/0016-7606(1998)110<0801:PSONRM>2.3.CO;2

Gusev, E., Rekant, P., Kaminsky, V., Krylov, A., Morozov, A., Shokalsky, S., & Kashubin, S. (2017). Morphology of seamounts at the Mendeleev Rise, Arctic ocean. *Polar Research*, *36*, 1298901. https://doi.org/10.1080/17518369.2017.1298901

Halbach, P., Segl, M., Puteanus, D., & Mangini, A. (1983). Co-fluxes and growth rates in ferromanganese deposits form Central Pacific seamount areas. *Nature*, *304*, 716–719. https://doi.org/10.1038/304716a0

Haley, B. A., Frank, M., Speilhagen, R. F., & Eisenhauer, A. (2008). Influence of brine formation on Arctic Ocean circulation over the past 15 million years. *Nature Geosciences*, *1*, 68–72. https://doi.org/10.1038/ngeo.2007.5

Hegewald, A., & Jokat, W. (2013). Relative sea level variation in the Chukchi region—Arctic Ocean—since the late Eocene. *Geophysical Research Letters*, *40*, 803–807. https://doi.org/10.1002/GRL.50182

Hein, J. R., Conrad, T. A., Frank, M., Christl, M., & Sager, W. W. (2012a). Copper-nickel-rich, amalgamated ferromanganese crust-nodule deposits from Shatsky Rise, NW Pacific. *Geochemistry, Geophysics, Geosystems*, *13*, Q10022. https://doi.org/10.1029/2012GC004286

Hein, J. R., Klofas, J. Mizell, K., & Conrad, T. A. (2012b). Rare-metal-rich ferromanganese mineral deposits from the western Arctic Ocean. Abstracts presented at 41st Underwater Mining Institute, Shanghai, China, October 15–20.

Hein, J. R., & Koschinsky, A. (2014). Deep-ocean ferromanganese crusts and nodules. In H. D. Holland and K. K. Turekian (Eds.), *Treatise on geochemistry* (2nd ed., Vol. 13, Chapter 11, pp. 273–291). Oxford, UK: Elsevier. https://doi.org/10.1016/B978-0-08-095975-7.01111-6

Hein, J. R., Koschinsky, A., Bau, M., Manheim, F. T., Kang, J. K., & Roberts, L. (2000). Cobalt-rich ferromanganese crusts in the Pacific. In D. S. Cronan (Ed.), *Handbook of marine mineral deposits* (pp. 239–279). Boca Raton, FL: CRC Press.

Hein, J. R., Koschinsky, A., & Halliday, A. N. (2003). Global occurrence of tellurium-rich ferromanganese crusts and a model for the enrichment of tellurium. *Geochimica Et Cosmochimica Acta*, *67*, 1117–1127. https://doi.org/10.1016/S0016-7037(02)01279-6

Hein, J. R., Koschinsky, A., & McIntyre, B. R. (2005). Mercury- and silver-rich ferromanganese-oxides, Southern California Borderland: Deposit model and environmental implications. *Economic Geology*, *100*, 1151–1168. https://doi.org/10.2113/gsecongeo.100.6.1151

Hein, J. R., Mizell, K., Koschinsky, A., & Conrad, T. A. (2013a). Deep-ocean mineral deposits as a source of critical metals for high- and green-technology applications: Comparison with land-based resources. *Ore Geology Reviews*, *51*, 1–14. https://doi.org/10.1016/j.oregeorev.2012.12.001

Hein, J. R., Normark, W. R., McIntyre, B. R., Lorenson, T. D., & Powell, C. L., II, (2006). Methanogenic calcite, ^{13}C-depleted bivalve shells, and gas hydrate from a mud volcano offshore southern California. *Geology*, *34*, 109–112. https://doi.org/10.1130/G22098.1

Hein, J. R., Schwab, W. C., & Davis, A. S. (1988). Cobalt and platinum-rich ferromanganese crusts and associated substrate rocks from the Marshall Islands. *Marine Geology*, *78*, 255–283. https://doi.org/10.1016/0025-3227(88)90113-2

Hein, J. R., Spinardi, F., Conrad, T. A., Conrad, J. E., & Genetti, J. (2013b). Critical metals in western Arctic Ocean ferromanganese mineral deposits. Abstract OS12B-06 presented at Fall Meeting, AGU, San Francisco, CA, December 9–13.

Hein, J. R., Spinardi, F., Okamoto, N., Mizell, K., Thorburn, D., & Tawake, A. (2015). Critical metals in manganese nodules from the Cook Islands EEZ, abundances and distributions. *Ore Geology Reviews*, *68*, 97–116. https://doi.org/10.1016/j.oregeorev.2014.12.011

Heller, M. I., Lam, P. J., Moffett, J. W., Till, C. P., Lee, J.-M., Toner, B. M., & Marcus, M. A. (2017). Accumulation of Fe oxyhydroxides in the Peruvian oxygen deficient zone implies non-oxygen dependent Fe oxidation. *Geochimica et Cosmochimica Acta*, *211*, 174–193.

Horner, T. J., Williams, H. M., Hein, J. R., Saito, M. A., Burton, K. W., Halliday, A. N., & Nielsen, S. G. (2015). Persistence of deeply sourced iron in the Pacific Ocean. *Proceedings of the National Academy of Sciences of the United States of America*, *112*(5), 1292–1297. https://doi.org/10.1073/pnas.1420188112

IASC. (2004). *International bathymetric chart of the Arctic Ocean (IBCAO)* (Research Publication RP-2). Boulder, CO: National Geophysical Data Center.

Jakobsson, M. (2002). Hypsometry and volume of the Arctic Ocean and its constituent seas. *Geochemistry, Geophysics, Geosystems*, *3*(5). https://doi.org/10.1029/2001GC000302

Jakobsson, M., Backman, J., Rudels, B., Nycander, J., Frank, M., Mayer, L., . . . Moran, K. (2007). The early Miocene onset of a ventilated circulation regime in the Arctic Ocean. *Nature*, *447*, 986–990. https://doi.org/10.1038/nature05924

Jokat, W., Ickrath, M., & O'connor, J. (2013). Seismic transect across the Lomonosov and Mendeleev Ridges: Constraints on the geological evolution of the Amerasia Basin, Arctic Ocean. *Geophysical Research Letters*, *40*, 5047–5051. https://doi.org/10.1002/grl.50975

Jones, E. P., Rudels, B., & Anderson, L. G. (1995). Deep waters of the Arctic Ocean: Origins and circulation. *Deep-Sea Research Part I: Oceanographic Research Papers*, *42*, 737–760. https://doi.org/10.1016/0967-0637(95)00013-V

Kamo, S. L., Czamansky, G. K., Amelin, Y., Fedorenko, V. A., Davis, D. W., & Trofimov, V. R. (2003). Rapid eruption of Siberian flood-volcanic rocks and evidence for coincidence with the Permian-Triassic boundary and mass extinction at 251 Ma. *Earth and Planetary Science Letters*, *214*, 75–91. https://doi.org/10.1016/S0012-821X(03)00347-9

Klovan, J. E., & Imbrie, J. (1971). An algorithm and FORTRAN-IV program for large-scale Q-mode factor analysis and calculation of factor scores. *Mathematical Geology*, *3*, 61–77. https://doi.org/10.1007/BF02047433

Klunder, M. B., Laan, P., Middag, R., de Baar, H. J. W., & Bakker, K. (2012). Dissolved iron in the Arctic Ocean: Important role of hydrothermal sources, shelf input and scavenging removal. *Journal of Geophysical Research*, *117*, CO4014. https://doi.org/10.1029/2011JC007135

Knauss, K., & Ku, T. L. (1983). The elemental composition and decay-series radio-nuclide content of plankton from the east Pacific. *Chemical Geology*, *39*, 125–145. https://doi.org/10.1016/0009-2541(83)90076-1

Kondo, Y., Obata, H., Hioki, N., Ooki, A., Nishino, S., Kikuchi, T., & Kuma, K. (2016). Transport of trace metals (Mn, Fe, Ni, Zn and Cd) in the western Arctic Ocean (Chukchi Sea and Canada Basin) in late summer 2012. *Deep-Sea Research Part I: Oceanographic Research Papers* , *116*, 236–252.

Konstantinova, N., Cherkashov, G., Hein, J. R., Mirão, J., Dias, L., Madureira, P., & Kuznetsov, V. (2017). Composition and characteristics of the ferromanganese crusts from the western Arctic Ocean. *Ore Geology Reviews*, *87*, 88–99. https://doi.org/10.1016/j.oregeorev.2016.09.011

Koschinsky, A., & Halbach, P. (1995). Sequential leaching of marine ferromanganese precipitates: Genetic implications. *Geochimica Et Cosmochimica Acta*, *59*, 5113–5132. https://doi.org/10.1016/0016-7037(95)00358-4

Koschinsky, A., & Hein, J. R. (2003). Uptake of elements from seawater by ferromanganese crusts: Solid-phase associations and seawater speciation. *Marine Geology*, *198*, 331–351. https://doi.org/10.1016/S0025-3227(03)00122-1

Kuzyk, Z. Z. A., Gobeil, C., Goñi, M. A., & Macdonald, R. W. (2017). Early diagenesis and trace element accumulation in North American Arctic margin sediments. *Geochimica et Cosmochimica Act*, *203*, 175–200. https://doi.org/10.1016/j.gca.2016.12.015

Lagerström, M. E., Field, M. P., Seguret, M., Fischer, L., Hann, S., & Sherrell, R. M. (2013). Automated on-line flow-injection ICP-MS determination of trace metals (Mn, Fe, Co, Ni, Cu and Zn) in open ocean seawater: Application to the GEOTRACES program. *Marine Chemistry*, *155*, 71–80. https://doi.org/10.1016/j.marchem.2013.06.001

Lee, C.–T. A., Cheng, X., & Horodyskyj, U. (2006). The development and refinement of continental arcs by primary basaltic magmatism, garnet pyroxenite accumulation, basaltic recharge and delamination: Insights from the Sierra Nevada, California. *Contributions to Mineralogy and Petrology*, *151*, 222–242. https://doi.org/10.1007/s00410-005-0056-1

Lundin, E. R., & Doré, A. G. (2017). The Gulf of Mexico and Canada Basin: Genetic siblings on either side of North America. *GSA Today*, *27*(1), 4–11. https://doi.org/10.1130/GSATG274A.1

Macdonald, R., & Gobeil, C. (2012). Manganese Sources and Sinks in the Arctic Ocean with Reference to Periodic Enrichments in Basin Sediments. *Aquatic Geochemistry*, *18*(6), 565–591.

Manheim, F. T., & Lane-Bostwick, C. M. (1988). Cobalt in ferromanganese crusts as a monitor of hydrothermal discharge on the sea floor. *Nature*, *335*, 59–62. https://doi.org/10.1038/335059a0

Martin, J.-M., & Meybeck, M. (1979). Elemental mass-balance of material carried by major world rivers. *Marine Chemistry*, *7*, 173–206. https://doi.org/10.1016/0304-4203(79)90039-2

Martinez, N. C., Murray, R. W., Dickens, G. R., & Kölling, M. (2009). Discrimination of sources of terrigenous sediment deposited in the central Arctic Ocean through the Cenozoic. *Paleoceanography*, *24*, PA1210. https://doi.org/10.1029/2007PA001567

Matthiessen, J., Knies, J., Vogt, C., & Stein, R. (2009). Pliocene palaeoceanography of the Arctic Ocean and subarctic seas. *Philosophical Transactions of the Royal Society A*, *367*, 21–48. https://doi.org/10.1098/rsta.2008.0203

Matveeva, T., Savvichev, A. S., Semenova, A., Logvina, E., Kolesnik, A. N., & Bosin, A. A. (2015). Source, origin, and spatial distribution of shallow sediment methane in the Chukchi Sea. *Oceanography*, *28*, 202–217. https://doi.org/10.5670/oceanog.2015.66

McLennan, S. M. (1989). Rare earth elements in sedimentary rocks: Influence of provenance and sedimentary processes. In B. R. Lipin and G. A. McKay (Eds.), *Geochemistry and mineralogy of rare earth elements* (pp. 169–200). Washington, DC: Mineralogical Society of America's Reviews in Mineralogy.

McManus, D. A., Kelley, J. C., & Creager, J. S. (1969). Continental shelf sedimentation in an Arctic environment. *Geological Society of America Bulletin*, *80*, 1961–1984.

Moran, K. J., Backman, H., Brinkhuis, S. C., Clemens, T., Cronin, G. R., Dickens, F., . . . Kristoffersen, Y. (2006). The Cenozoic palaeoenvironment of the Arctic Ocean. *Nature*, *441*, 601–605. https://doi.org/10.1038/nature04800

Moran, S. B., & Moore, R. M. (1992). Kinetics of the removal of dissolved aluminum by diatoms in seawater: A comparison with thorium. *Geochimica et Cosmochimica Acta*, *56*, 3365–3374. https://doi.org/10.1016/0016-7037(92)90384-U

Morozov, A. F., Petrov, O. V., Shokalsky, S. P., Kashubin, S. N., Kremenetsky, A. A., Shkatov, M. Y., . . . Shatov, V. V. (2013). New Geological data are confirming continental origin of the central Arctic rises [in Russian]. *Regionalnaya Geologia i Metallogenia (Regional Geology and Metallogeny)*, *53*, 34–55.

Mukasa, S., Andronikov, A., Mayer, L., & Brumley, K. (2009). Geochemistry and geochronology of the first intraplate lavas recovered from the Arctic Ocean. *Geological Society of America Abstracts with Programs*, *41*(7), 370.

Nielsen, S. G., Mar-Gerrison, S., Gannoun, A., LaRowe, D., Klemm, V., Halliday, A. N., . . . Hein, J. R. (2009). Thallium isotope evidence for a permanent increase in marine organic carbon export in the early Eocene. *Earth and Planetary Science Letters*, *278*, 297–307. https://doi.org/10.1016/j.epsl.2008.12.010

Nozaki, T., Takumaru, A., Takaya, Y., Kato, Y., Suzuki, K., & Urabe, T. (2016). Major and trace element compositions and resource potential of ferromanganese crust at Takuyo Daigo Seamount, northwestern Pacific Ocean. *Geochemical Journal*, *50*, 527–537. https://doi.org/10.1038/304716a0

Oakey, G. N., & Saltus, R. W. (2016). Geophysical analysis of the Alpha-Mendeleev ridge complex: Characterization of the High Arctic Large Igneous Province. *Tectonophysics*, *691*, 65–84. https://doi.org/10.1016/j.tecto.2016.08.005

O'Brien, T. M., Miller, E. L., Benowitz, J. P., Meisling, K. E., & Dumitru, T. A. (2016). Dredge samples from the Chukchi Borderland: Implications for paleogeographic reconstruction and tectonic evolution of the Amerasia Basin of the Arctic. *American Journal of Science*, *316*, 873–924. https://doi.org/10.2475/09.2016.03

Ohnemus, D. C., Auro, M. E., Sherrell, R. M., Lagerstrom, M., Morton, P. L., Twining, B. S., . . . Lam, P. J. (2014). Laboratory intercomparison of marine particulate digestions including Piranha: A novel chemical method for dissolution of polyethersulfone filters. *Limnology and Oceanography: Methods*, *12*, 530–547. https://doi.org/10.4319/lom.2014.12.530

Ohnemus, D. C., & Lam, P. J. (2015). Cycling of lithogenic marine particles in the US GEOTRACES North Atlantic transect. *Deep Sea Research Part II: Topical Studies in Oceanography*, *116*, 283–302.

Parker, C. E., Brown, M. T., & Bruland, K. W. (2016). Scandium in the open ocean: A comparison with other group 3 trivalent metals. *Geophysical Research Letters*, *43*, 2758–2764. https://doi.org/10.1002/2016GL067827

Pease, V., Drachev, S., Stephenson, R., & Zhang, X. (2014). Arctic lithosphere—A review. *Tectonophysics*, *628*, 1–25. https://doi.org/10.1016/j.tecto.2014.05.033

Pichocki, C., & Hoffert, M. (1987). Characteristics of Co-rich ferromanganese nodules and crusts sampled in French Polynesia. *Marine Geology*, *77*, 109–119.

Pisias, N. G., Murray, R. W., & Scudder, R. P. (2013). Multivariate statistical analysis and partitioning of sedimentary geochemical data sets: General principles and specific MATLAB scripts. *Geochemistry, Geophysics, Geosystems*, *14*, 4015–4020. https://doi.org/10.1002/ggge.20247

Planquette, H., & Sherrell, R. M. (2012). Sampling for particulate trace element determination using water sampling bottles: Methodology and comparison to in situ pumps. *Limnology and Oceanography: Methods*, *10*(5), 367–388. https://doi.org/10.4319/lom.2012.10.367

Raiswell, R. (2011). Iron transport from the continents to the open ocean: The aging-rejuvenation cycle. *Elements*, *7*, 101–106.

Rogers, H. J., Synge, C., & Woods, V. E. (1980). Antibacterial effect of scandium and indium complexes of enerochelin on Klebsiella pneumonia. *Antimicrobial Agents and Chemotherapy*, *18*(1), 63–68. https://doi.org/10-1128/AAC.18.1.63

Rudnick, R. L., & Gao, S. (2003). Composition of the continental crust. In *Treatise on geochemistry* (Vol. 3, pp. 1–64). Amsterdam, the Netherlands: Elsevier.

Santschi, P. H., Murray, J. W., Baskaran, M., Benitez-Nelson, C. R., Guo, L. D., Hung, C.-C., . . . Roy-Barman, M. (2006). Thorium speciation in seawater. *Marine Chemistry*, *100*, 250–268. https://doi.org/10.1016/j.marchem.2005.10.024

Scott, D. B., Mudie, P. J., Baki, V., MacKinnon, K. D., & Cole, F. E. (1989). Biostratigraphy and late Cenozoic paleoceanography of the Arctic Ocean: Foraminiferal lithostratigraphic, and isotopic evidence. *Geological Society of America Bulletin*, *101*, 260–277. https://doi.org/10.1130/0016-7606(1989)101<0260:BALCPO>2.3.CO;2

Sharma, M., Basu, A. R., & Nesterenko, G. V. (1991). Nd-Sr isotopes, petrochemistry, and origin of the Siberian flood basalts, USSR. *Geochimica et Cosmochimica Acta*, *55*, 1183–1192. https://doi.org/10.1016/0016-7037(91)90177-7

Shimeld, J., Li, Q., Chian, D., Lebedeva-Ivanova, N., Jackson, R., Mosher, D., & Hutchinson, D. (2016). Seismic velocities within the sedimentary succession of the Canada Basin and southern Alpha-Mendeleev Ridge, Arctic Ocean: Evidence for accelerated porosity reduction? *Geophysical Journal International*, *204*, 1–20. https://doi.org/10.1093/gji/ggv416

So, C.-S. (1978). Geochemistry and origin of amphibolite and magnetite from the Yangyang iron deposit in the Gyeonggi Metamorphic Complex, *Republic of Korea*. *Mineralium Deposita*, *13*, 105–117. https://doi.org/10.1007/BF00202910

St. John, K. (2008). Cenozoic ice-rafting history of the central Arctic Ocean: Terrigenous sands on the Lomonosov Ridge. *Paleoceanography*, *23*, PA1S05. https://doi.org/10.1029/2007PA001483

Taylor, S. R., & McLennan, S. M. (1985). *The continental crust: Its composition and evolution*. Oxford, UK: Blackwell. https://doi.org/10.1002/gj.3350210116

Timmermans, M.-L., Winsor, P., & Whitehead, J. A. (2005). Deep-water flow over the Lomonosov Ridge in the Arctic Ocean. *Journal of Physical Oceanography*, *35*, 1489–1493. https://doi.org/10.1175/JPO2765.1

Trimble, S. M., Baskaran, M., & Procelli, D. (2004). Scavenging of thorium isotopes in the Canada Basin of the Arctic Ocean. *Earth and Planetary Science Letters*, *222*, 915–932. https://doi.org/10.1016/j.epsl.2004.03.027

Van der Loeff, M. R., Cai, P., Stimac, I., Bauch, D., Hanfland, C., Roeske, T., & Moran, S. B. (2012). Shelf-basin exchange times of Arctic surface waters estimated from ^{228}Th/^{228}Ra disequilibrium. *Journal of Geophysical Research*, *117*, C03024. https://doi.org/10.1029/2011JC007478

Van Wagoner, N. A., Williamson, M.-C., Robinson, P. T., & Gibson, I. L. (1986). First samples of acoustic basement recovered from the Alpha Ridge, Arctic Ocean: New constraints for the origin of the ridge. *Journal of Geodynamics*, *6*, 177–196. https://doi.org/10.1016/0264-3707(86)90038-4

Vedamati, J., Goepfert, T., & Moffett, J. W. (2014). Iron speciation in the eastern tropical South Pacific oxygen minimum zone off Peru. *Limnology and Oceanography*, *59*, 1945–1957. https://doi.org/10.4319/lo.2014.59.6.1945

Vernikovsky, V. A., Morozov, A. F., Petrov, O. V., Travin, A. V., Kashubin, S. N., Shokal'sky, S. P., . . . Petrov, E. O. (2014). New data on the age of dolerites and basalts of Mendeleev Rise (Arctic Ocean). *Doklady Earth Sciences*, *454*(Part 2), 97–101. https://doi.org/10.1134/S1028334X1402007X

Viscosi-Shirley, C., Pisias, N., & Mammone, K. (2003). Sediment source strength, transport pathways and accumulation patterns on the Siberian-Arctic's Chukchi and Laptev shelves. *Continental Shelf Research*, *23*, 1201–1225. https://doi.org/10.1016/S0278-4343(03)00090-6

Vonk, J. E., Giosan, L., Blusztajn, J., Montlucon, D., Pannatier, E. G., McIntyre, C., . . . Eglinton, T. I. (2015). Spatial variations in geochemical characteristics of the modern Mackenzie delta sedimentary system. *Geochimica et Cosmochimica Acta*, *171*, 100–120. https://doi.org/10.1016/j.gca.2015.08.005

Wegorzewski, A. V., Kuhn, T., Dohrmann, R., Wirth, R., & Grangeon, S. (2015). Mineralogical characterization of individual growth structures of Mn-nodules with different Ni+Cu content from the central Pacific Ocean. *American Mineralogist*, *100*, 2497–2508.

Wen, X., De Carlo, E. H., & Li, Y. H. (1997). Interelement relationships in ferromanganese crusts from the central Pacific ocean: Their implications for crust genesis. *Marine Geology*, *136*, 277–297. https://doi.org/10.1016/S0025-3227(96)00064-3

Winter, B. L., Johnson, C. M., & Clark, D. L. (1997). Geochemical constraints on the formation of Late Cenozoic ferromanganese micronodules from the central Arctic Ocean. *Marine Geology*, *138*, 149–169. https://doi.org/10.1016/S0025-3227(97)00013-3

Wooden, J. L., Czamanske, G. K., Fedorenko, V. A., Arndt, N. T., Chauvel, C., Bouse, R. M., . . . Siems, D. F. (1993). Isotopic and trace-element constraints on mantle and crustal contributions to Siberian continental flood basalts, Noril'sk area, Siberia. *Geochimica et Cosmochimica Acta*, *57*, 3677–3704. https://doi.org/10.1016/0016-7037(93)90149-Q